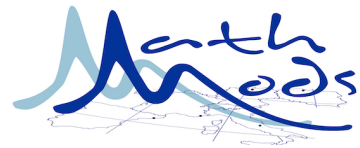




POLITECHNIKA
GDAŃSKA



MASTER'S THESIS

FE Model of Moisture Absorption by Adhesive Joints between Composites

Author:

Verónica Bonilla Mora

Supervisor:

Magdalena Mieloszyk
Ph.D., Eng.

*A thesis submitted in fulfillment of the requirements for the
Erasmus Mundus Double Master's Degree Programme in
Mathematical Modelling in Engineering: Theory, Numerics, Applications*

in the

Faculty of Applied Physics and Mathematics
Department of Solid State Physics

October, 2016



POLITECHNIKA GDAŃSKA



UNIVERSITÀ DEGLI STUDI
DELL' AQUILA

Erasmus Mundus Consortium “MathMods”

Double Master’s Degree Programme in
Mathematical Modelling in Engineering: Theory, Numerics, Applications

Master of Science in
Technical Physics
Specialization Advanced Computational
Methods in Materials Science

POLITECHNIKA GDAŃSKA

Laurea Magistrale in
Ingegneria Matematica

UNIVERSITÀ DEGLI STUDI DELL' AQUILA

In the framework of the
Consortium Agreement and Award of a Joint/Multiple Degree 2013-2019

Master’s thesis

FE Model of Moisture Absorption by Adhesive Joints between Composites

Supervisor

Magdalena Mieloszyk
Ph.D., Eng.

Candidate

Verónica Bonilla Mora
Matricola: 238831

2014/2016



**GDAŃSK UNIVERSITY
OF TECHNOLOGY**

FACULTY OF APPLIED PHYSICS AND MATHEMATICS

Student's name and surname: Verónica Bonilla Mora
ID: 164308
Second cycle studies
Mode of study: Full-time studies
Field of study: Technical Physics
Specialization: Advanced Computational Methods in Materials Science

MASTER'S THESIS

Title of thesis:

FE Model of Moisture Absorption by Adhesive Joints between
Composites

Title of thesis (in Polish):

Modelowanie metodą elementów skończonych absorpcji wilgoci w
połączeniach klejowych między elementami kompozytowymi

Supervisor	Head of Department
<i>signature</i>	<i>signature</i>

Date of thesis submission to faculty office:



**GDAŃSK UNIVERSITY
OF TECHNOLOGY**

FACULTY OF APPLIED PHYSICS AND MATHEMATICS

STATEMENT

First name and surname: Verónica Bonilla Mora
 Date and place of birth: 30.01.1988, San José
 ID: 164308
 Faculty: Faculty of Applied Physics and Mathematics
 Field of study: technical physics
 Cycle of studies: postgraduate studies
 Mode of studies: Full-time studies

I, the undersigned, agree that my diploma thesis entitled: "FE Model of Moisture Absorption by Adhesive Joints between Composites" may be used for scientific or didactic purposes.¹

Gdańsk,

.....
signature of the student

Aware of criminal liability for violations of the Act of 4th February 1994 on Copyright and Related Rights (Journal of Laws 2006, No. 90, item 631) and disciplinary actions set out in the Law on Higher Education (Journal of Laws 2012, item 572 with later amendments),² as well as civil liability, I declare that the submitted diploma thesis is my own work.

This diploma thesis has never before been the basis of an official procedure associated with the awarding of a professional title.

All the information contained in the above diploma thesis which is derived from written and electronic sources is documented in a list of relevant literature in accordance with art. 34 of the Copyright and Related Rights Act.

I confirm that this diploma thesis is identical to the attached electronic version.

Gdańsk,

.....
signature of the student

I authorise the Gdańsk University of Technology to include an electronic version of the above diploma thesis in the open, institutional, digital repository of the Gdańsk University of Technology and for it to be submitted to the processes of verification and protection against misappropriation of authorship.

Gdańsk,

.....
signature of the student

¹ Decree of Rector of Gdańsk University of Technology No. 34/2009 of 9th November 2009, TUG archive instruction addendum No. 8.

² Act of 27th July 2005, Law on Higher Education:

Art. 214, section 4. Should a student be suspected of committing an act which involves the appropriation of the authorship of a major part or other elements of another person's work, the rector shall forthwith order an enquiry.

Art. 214 section 6. If the evidence collected during an enquiry confirms that the act referred to in section 4 has been committed, the rector shall suspend the procedure for the awarding of a professional title pending a judgement of the disciplinary committee and submit formal notice of the committed offence.

GDAŃSK UNIVERSITY OF TECHNOLOGY

Abstract

Faculty of Applied Physics and Mathematics
Department of Solid State Physics

Erasmus Mundus Double Master's Degree in
Mathematical Modelling in Engineering

FE Model of Moisture Absorption by Adhesive Joints between Composites

by Verónica Bonilla Mora

Adhesive joints offer many advantages over traditional mechanical joining systems. Nonetheless, their use is limited since they can be adversely affected by extreme temperatures and humidity conditions. Moisture absorption in an adhesive can alter its tensile strength and compromise the structural integrity of the joint. Thus, moisture absorption and moisture-induced strain monitoring is an area of high interest in the field of structural health monitoring (SHM).

In the present project, several finite element models were created to analyse the thermal response, diffusion dynamics and strain development of two adhesive joints with different thickness size between composites; and serve as a methodology for future studies in the area. The project was motivated by experimental results obtained by the Institute of Fluid-Flow Machinery, in which Fiber-Bragg grating sensors were used to monitor the moisture-induced strains on the adhesive joints.

Three main analyses were performed: a thermal analysis, a mass diffusion analysis and a hygro-mechanical analysis. All three were developed through the use of the FE software Abaqus. Simulation results were validated by experimental data.

Acknowledgements

The completion of any project invariably involves the collaboration of many helping hands at different stages. This project wasn't the exception, and I was lucky to count on wonderful people along the way.

A special thanks to my supervisor, for always taking the time to promptly respond my many, many emails and patiently answering my, also, many, many questions. And my eternal gratitude to Rohan Soman, part of the IMP PAN team, for taking the time to discuss my models and results.

My sincerest thanks to professor Jerzy Bobinski, for helping me pass the first technical hurdles of this project.

And Adwait, your positivism and excitement to learn was always a source of motivation throughout this whole experience. Thank you for helping me "see the light" despite being miles and miles away, in true MathMods fashion. Too good, man!

The work in this thesis was inspired by and conducted in collaboration with the IMP PAN team realising the project entitled: 'Quality assurance concepts for adhesive bonding of aircraft composite structures by advanced NDT' (Com-BoNDT). This project has received funding from the European Union's Horizon 2020 research and innovation programme under grant agreement No 636494.

The research was supported by the project entitled: Non-invasive Methods for Assessment of Physicochemical and Mechanical Degradation (PBS1/B6/8/2012) granted by National Centre for Research and Development in Poland.

Contents

Abstract	ix
Acknowledgements	xi
1 Moisture-induced strain monitoring	1
1.1 Introduction	1
1.2 Fiber-Bragg Grating Sensors	2
1.2.1 Strain sensitivity	3
1.2.2 Temperature Sensitivity	4
1.3 Experimental Results	5
1.3.1 Moisture Content	5
1.3.2 Temperature-Induced Strains	7
1.3.3 Moisture-Induced Strain Results	8
1.4 Hypothesis and Main Objectives	10
2 Thermal Analysis	11
2.1 Introduction	11
2.2 Mathematical Model	11
2.3 Thermal Simulation	13
2.3.1 Simulation - Dry Conditions	16
2.3.2 Simulation - Wet Conditions	17
2.4 Conclusions	19
3 Mass Diffusion Analysis	21
3.1 Introduction	21
3.2 Moisture Diffusion	22
3.2.1 Time-Varying Boundary Conditions	24
3.2.2 Dual-Stage Model	25
3.3 Weak form discretization	26
3.4 Diffusion Model	27
3.4.1 Material Properties	27
Time-Varying Boundary Conditions	27
Dual-Stage	28
3.4.2 Boundary Conditions	29
Time-Varying Boundary Conditions	29
Dual-Stage Model	30
3.4.3 Model Mesh	31
3.5 Results	32
3.5.1 Average Concentration - Whole Sample	33
3.5.2 1 mm vs 0.5 mm Mesh	34

3.5.3	Average Concentration - Sample A and B	35
3.5.4	Average Concentration - Sensor Areas	35
3.5.5	Concentration Distribution	36
3.6	Conclusions	37
4	Hygro-Mechanical Analysis	41
4.1	Introduction	41
4.2	Hygroscopic and Thermal Strain	42
4.3	Hygro-Mechanical Model	43
4.3.1	Coupling the Mass Diffusion Analysis	43
4.3.2	Material Properties	43
4.3.3	Boundary Conditions and Loads	45
4.3.4	Interactions	46
4.3.5	Model Mesh	46
4.4	Analysis Results	47
4.4.1	Time-Varying BC Strain Profiles	48
4.4.2	Dual-Stage Strain Profiles	49
4.4.3	1 mm vs 0.5 mm Mesh	50
4.4.4	Water Pressure Effect	51
4.5	Conclusions	53
5	Summary	57
5.1	Introduction	57
5.1.1	Thermal Analysis	57
5.1.2	Mass Diffusion Analysis	58
5.2	Hygro-mechanical Analysis	59
5.3	Future Works	60
A	User Subroutine - UFIELD	61
B	Average Concentration - Python Script	63
C	Record Key Change Code	65
	Bibliography	69

Dedicated to my loving parents,

Raúl and Sylvia

*"It's away from home when you realize the true meaning of a
parent's love and the significance of family."*

Anonymous

Chapter 1

Moisture-induced strain monitoring

1.1 Introduction

Composites are, like their name suggests, materials composed of two or more different materials joined together to create a new material with special and unique characteristics. They have been widely used by mankind for centuries, with the earliest composites being plywood, cartonnage, concrete, and mortar; among others [1].

In recent years, composite manufacturing has evolved to create materials by merging several different layers of fibres and resins. The layers can be chosen to obtain materials with the required structural and mechanical qualities for specific applications. Most notably, to create materials that possess higher strength, more corrosion resistance and better stiffness-to-weight ratios than other traditional materials like metals [2, 3]. As such, the market of composite materials has bloomed and their use can be found in almost all industries in the world, from aeronautics to construction, to medicine, to the oil and gas industry [4, 5]. Clearly, the study of composites as well as their structures is of utmost importance for designers and manufacturers to guarantee needed safety standards and increase reliability.

A widely used method for composite structure manufacturing is the use of high strength adhesive joining. Adhesive joints are preferable to traditional methods like mechanical fasteners that may require the drilling of the composite. Drilling holes could be a source of damage for the material and it introduces undesired stress concentrations near the hole [6]. Adhesive bonds are also lighter than riveting or welding methods, present higher fatigue resistance and can distribute loads over larger areas [7].

Of course, when employing these types of joints, care has to be given to the type of adhesives used, surface preparation and environmental conditions where the structure will be used. Due to the polymeric nature of adhesives, adhesive joints present limited resistance to extreme temperature and humidity conditions [8]. As several studies have shown [3, 9-11], moisture can be a major contributing factor to adhesive joint and composite failure. Moisture absorption by an adhesive leads to several changes in its physical and mechanical structure. It reduces the transition temperature T_g , reduces tensile strength and lowers the ultimate elongation of the adhesive [11]. Thus, moisture absorption and moisture-induced strain monitoring is an area of high interest in the field of structural health monitoring (SHM).

The present project was motivated by experimental results obtained at the Institute of Fluid-Flow Machinery in Gdańsk, Poland. The experiment made use of fiber Bragg grating sensors to quantify developed strains caused by moisture absorption of an epoxy paste adhesive used to join two composite materials [12]. In the present project, a finite element model was generated to simulate the thermal response, diffusion dynamics and strain development of the tested components and serve as a methodology for future studies in the area.

1.2 Fiber-Bragg Grating Sensors

Fiber Bragg Grating sensors are optical sensors whose core index of refraction has been altered by optical absorption of UV light. Their use has become widespread due to the many advantages they possess: small dimensions, light weight, insensitivity to electromagnetic interference, multiplexing capabilities and resistance to corrosion [13].

The core index of refraction is changed in a periodic pattern along the core of the fibers creating phase structures, or phase gratings [14]. When light interacts with the gratings created inside the fiber core, only a small part of the light spectrum will be reflected back. The reflected spectrum is centred on the Bragg-wavelength (λ_B) and depends on the effective index of refraction (n_{eff}) and on the spacing between gratings, the Bragg period (Λ), as stated by the Bragg condition [13]:

$$\lambda_B = 2n_{eff}\Lambda \quad (1.1)$$

Applied mechanical strains and temperature changes affect FBG wavelength measurements, which is why it is possible and have been regularly used for strain and temperature monitoring [13, 15–17]. Parting from equation 1.1, the change of the Bragg-wavelength due to strain and temperature changes is,

$$\Delta\lambda_B = 2 \left(\Lambda \frac{\partial n}{\partial \epsilon} + n \frac{\partial \Lambda}{\partial \epsilon} \right) \Delta\epsilon + 2 \left(\Lambda \frac{\partial n}{\partial T} + n \frac{\partial \Lambda}{\partial T} \right) \Delta T \quad (1.2)$$

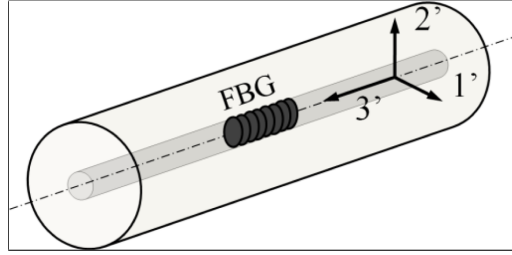


FIGURE 1.1: Fiber Bragg Grating Sensor Diagram [18]

1.2.1 Strain sensitivity

The first term of equation 1.2 is related to the strain contribution to the wavelength measurement. The change in the refractive index of the fibre due to strain in the longitudinal axis is the following

$$\partial n_{3'} = -\frac{n_{eff}^2}{2} [\rho_{13}\epsilon_{1'} + \rho_{23}\epsilon_{2'} + \rho_{33}\epsilon_{3'}] \quad (1.3)$$

where ρ_{13} , ρ_{23} and ρ_{33} are the elements of the strain-optic tensor of a homogeneous orthotropic material [19] following the coordinate system shown on figure 1.1. The change in the Bragg period is $\partial\Lambda = \Lambda_0(1 + \epsilon_{3'})$ [17], therefore, the wavelength response to axial strains can be expressed as follows [20]

$$\frac{\Delta\lambda_B}{\lambda_B} = \left[1 - \frac{1}{2} n_{eff}^2 [\rho_{12} - \nu(\rho_{11} + \rho_{12})] \right] \epsilon_{3'} = (1 - \rho_\epsilon) \epsilon_{3'} \quad (1.4)$$

where ρ_ϵ is an effective strain-optic coefficient of the fiber optic material which can be measured experimentally and is defined on equation 1.5.

$$\rho_\epsilon = \frac{n_{eff}^2}{2} [\rho_{12} - \nu(\rho_{11} + \rho_{12})] \quad (1.5)$$

where ρ_{11} and ρ_{12} are components of the strain-optic tensor, n_{eff} is the index of the fiber core, and ν is Poisson's ratio [13]

For silica fiber sensors, the wavelength-strain sensitivities of 800 nm and 1550 nm FBGs have been measured as $\sim 0.64 \text{ pm } \mu\epsilon^{-1}$ and $\sim 1.15 \text{ pm}^{-1} \mu\epsilon$ [21]. The manufacturer of the FBG sensors used in the experiment states that $(1 - \rho_\epsilon)$ has a value of 0.890 [12].

1.2.2 Temperature Sensitivity

The rest of equation 1.2 corresponds to the effect of temperature on the wavelength measurements. It can be rewritten as follows,

$$\frac{\Delta\lambda_B}{\lambda_B} = \left[\frac{1}{n_{eff}} \frac{\partial n_{eff}}{\partial T} + \frac{1}{\Lambda} \frac{\partial \Lambda}{\partial T} \right] \Delta T \quad (1.6)$$

The first term in the brackets is known as the thermal expansion coefficient, α_f , of the fiber core (equation 1.7). For silica it has an approximate value of $0.55 \times 10^{-6} \text{ 1/K}$ [18]. The second term represents the thermo-optic coefficient, α_n , (equation 1.8). It is dependant on the type and concentration of dopants in the sensor [18]. For germanium-doped, silica-core fibers values have been found to be between 3.0×10^{-6} [22] and $8.6 \times 10^{-6} \text{ 1/K}$ [13].

$$\alpha_f = \frac{1}{n_{eff}} \frac{\partial n_{eff}}{\partial T} \quad (1.7)$$

$$\alpha_n = \frac{1}{\Lambda} \frac{\partial \Lambda}{\partial T} \quad (1.8)$$

Sometimes in the literature, the thermal expansion coefficient and the thermo-optic coefficient can be found combined as the so-called temperature coefficient, $\beta = \alpha_f + \alpha_n$. Equation 1.6 then, can be rewritten as,

$$\frac{\Delta\lambda_B}{\lambda_B} = \beta \Delta T \quad (1.9)$$

For a silica fiber, the wavelength-temperature sensitivities of 800 nm and 1.5 μm FBGs have been measured with values of ~ 6.8 and $\sim 13 \text{ pm}/^\circ\text{C}$, respectively [21].

1.3 Experimental Results

One of the focus areas of the Mechanics of Intelligent Structures Department at the Institute of Fluid-Flow Machinery is the static and dynamics of composite structures and possible failure modes [23]. As part of those investigation efforts, experimental results were obtained for the moisture-induced strains on an adhesive joint between composites.

1.3.1 Moisture Content

The main purpose of the investigation was to determine the applicability and feasibility of using FBG (Fiber Bragg Grating) sensors for structural health monitoring of moisture contamination of adhesive bonds in composite structures [12].

The experiment consisted of three different samples denominated A, B and C. Each sample was made up of two GFRP (Glass Fiber Reinforced Plastic) composites with a stacking sequence of (0/90/0/90/90/0/90/0) and sizes of 250x50x1 mm (figure 1.2).

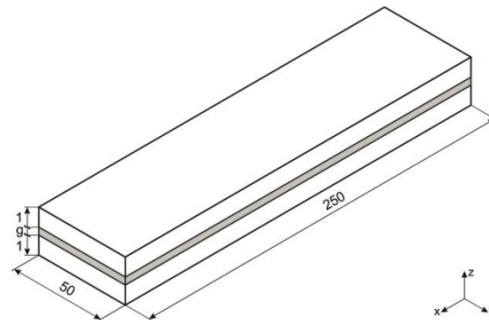


FIGURE 1.2: Sample Dimensions [12]

The composites were bonded together by a 0.2 mm layer of adhesive (in the case of sample B, the adhesive layer had a thickness of 0.4 mm). FBG sensors were placed in the adhesive layer, with their placement varying within samples as shown on figure 1.3.

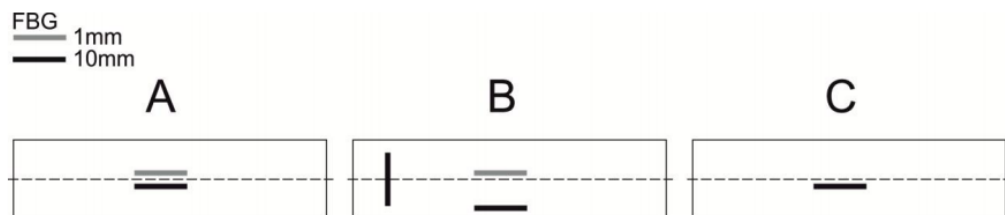


FIGURE 1.3: FBG sensor placement [12]

The adhesive used was a two-part structural epoxy paste adhesive produced by Henkel Corporation and commercially known as Loctite EA 9394 Aero or Hysol EA 9394. Its main properties as listed by the manufacturer [24] are given on Table 1.1.

TABLE 1.1: Adhesive Properties

Parameter	Value	Units
T_g (dry)	78	°C
T_g (wet)	68	°C
Tensile Strength at 25°C	46	MPa
Tensile Modulus at 25°C	4.237	GPa
Elongation at 25°C at break	0.017	%
Compressive Strength at 25°C	68.9	MPa
Cure Temperature	25-93	°C
Cure Time	3-5	day

After proper curing, the assembled samples were placed into individual boxes and submerged in demineralized water. The samples were kept inside a temperature chamber at $60^\circ\text{C} \pm 2^\circ\text{C}$ for approximately 2 weeks. During that time, the moisture content was regularly monitored by weighing the samples and calculating it by the following equation,

$$M(t) = \frac{W(t) - W_o}{W_o} \cdot 100 \quad (1.10)$$

where $W(t)$ is the measured weight at a given time and W_o is for the initially dry weight of the sample.

After the two weeks, the moisture content of the samples was around 2.26%. Figure 1.4 shows the moisture weight-gain against time.

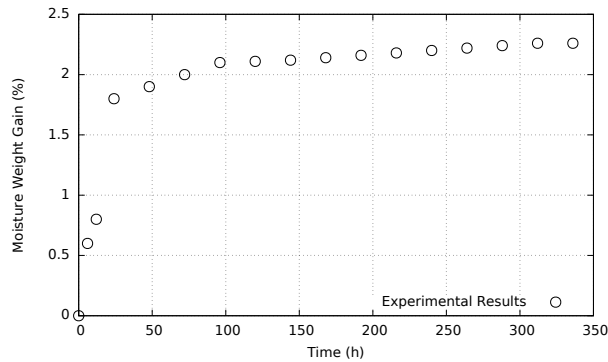


FIGURE 1.4: Moisture Weight Gain (%)

1.3.2 Temperature-Induced Strains

As mentioned earlier, FBG sensors are very sensitive to temperature changes. In order to experimentally quantify only the moisture-induced strains (ϵ) on the adhesive bond, it was necessary to determine the temperature contribution, ϵ_T , to the total values measured, ϵ_C .

$$\epsilon_C = \epsilon_T + \epsilon \quad (1.11)$$

To do so, dry samples were placed in a heating chamber at 60 ± 2 °C. The temperature was monitored using a temperature probe (os4200, Micron Optics). Figure 1.5 shows the temperature measurements of both, the 1 mm and 10 mm FBG sensors.

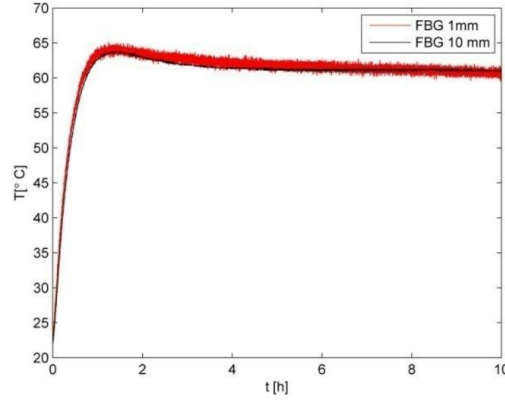


FIGURE 1.5: FBG sensors temperature measurements [12]

The total strain values, ϵ_C , can be determined from the FBG readings using equation 1.12 [12].

$$\epsilon_C(t) = \frac{\lambda_{mi}(t) - \lambda_b}{(1 - \rho_\epsilon)\lambda_b} \quad (1.12)$$

where λ_B is the base Bragg wavelength, λ_{mi} is the Bragg wavelength from the i -th measurement and ρ_ϵ is the effective strain-optic coefficient.

In this case, since the measurements are on dry samples, the total measured strains correspond to the temperature-induced strains. The relationship between strain and temperature is given by equation 1.13, where p is the volumetric expansion coefficient that depends on the fiber optic and adhesive materials. The value of p for the samples used was determined to be $9.15 \mu\epsilon/^\circ\text{C}$ with the experimental data gathered.

$$\epsilon_T = p\Delta T(t) \quad (1.13)$$

1.3.3 Moisture-Induced Strain Results

The information gathered from the temperature-induced strains allows the quantification of the moisture-induced strains by equation 1.14.

$$\epsilon = \epsilon_C - \epsilon_T \quad (1.14)$$

The samples were submerged in demineralise water and kept in a temperature chamber at 60 ± 2 °C for two weeks. Total strain measurements were calculated from the FBG readings using equation 1.12. The temperature-induced strains were calculated by equation 1.13, so that the moisture-induced strains could be determined with equation 1.14. Figure 1.6 shows the measured strains on samples A and B against time.

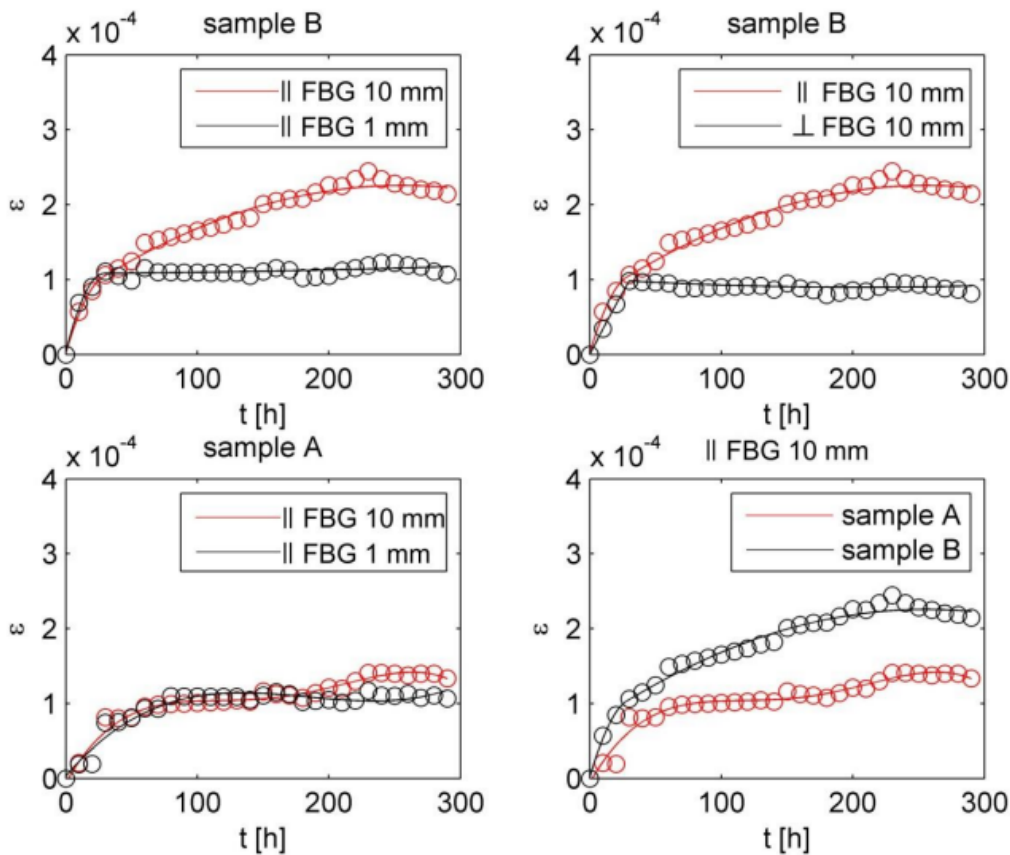


FIGURE 1.6: Moisture-induced strains on A and B Samples [12]

Figure 1.7 shows the moisture-induced versus the water concentration on the samples. These results show that FBG sensors perpendicular to longer axis (sample B, figure 1.3) as well as 1 mm FBG sensors are not adequate for strain measurement when the moisture intake is higher than 1.5% of the sample weight [12]. The length of the sensor and the location for the 1 mm and 10 mm FBG sensor, respectively, may be the cause. On the other hand, 10 mm FBG sensors parallel to the longer axis allow to determine the amount of moisture in the adhesive layer within the considered range of 0 to 2% of the sample weight.

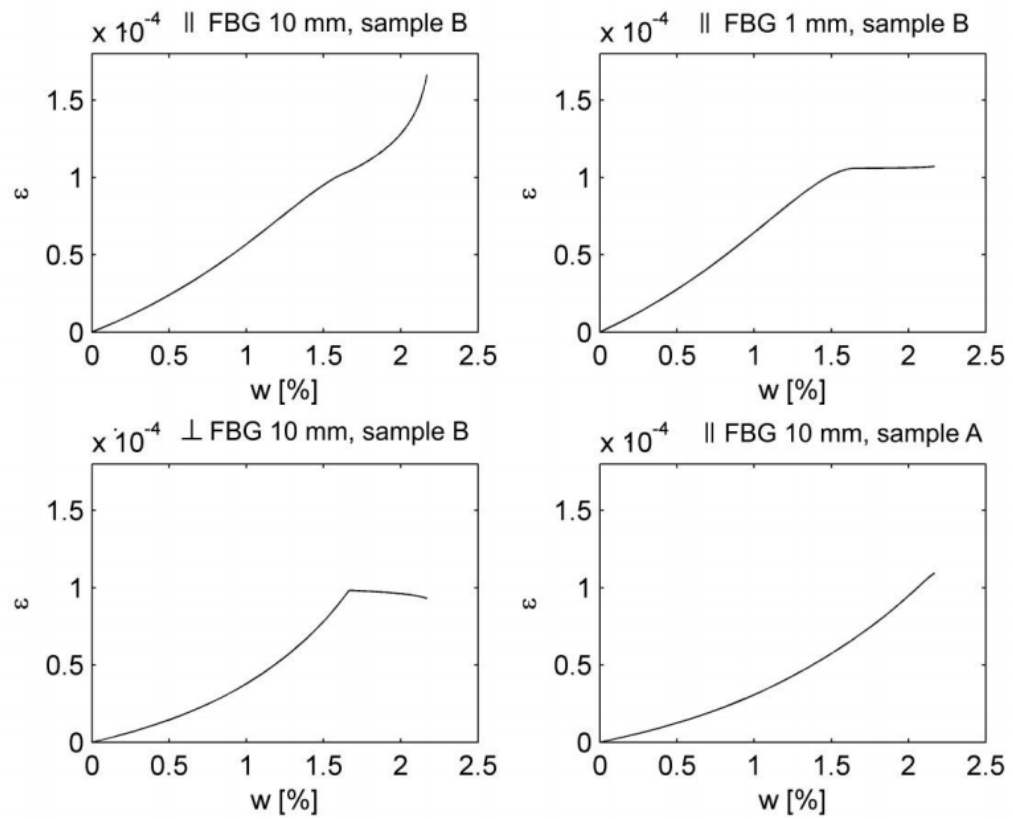


FIGURE 1.7: Moisture-induced strains vs water concentration [12]

1.4 Hypothesis and Main Objectives

The absorption of moisture by an adhesive joint, may greatly affect the adhesive's chemical composition and mechanical strength; compromising the assembly's structural integrity. The use of embedded FBG sensors adhesive joints could help determine working conditions in real time, preventing mechanical failures and allowing the use of adhesive joints in a wider array of applications where they haven't been used due to safety concerns.

Based on literature review, experimental investigations conducted at the IMP PAN, as well as my own observations; the hypothesis for the present project is that:

Numerical simulations, in particular finite element (FE) models, can be used to better understand the complex dynamics between moisture absorption and hygroscopic strain distribution in an adhesive layer.

The aim of project is to perform three different numerical analyses to simulate the different conditions the experimental samples presented: a thermal analysis, a mass diffusion analysis and a hygro-mechanical analysis. Another goal of the project is to serve as a methodology for future research in the field. All three analyses will be conducted through the use of the finite element method using the commercial code Abaqus as the main computational tool. Experimental results from samples A and B, as classified in figure 1.3, will be used to compare and validate the numerical findings.

Chapter 2

Thermal Analysis

2.1 Introduction

A thermal analysis is the analysis of a system using the laws of heat transfer. It allows to quantify the heat transfer rate and temperature distribution in the system. As previously mentioned, during the experiment, each sample was placed in an individual box inside a temperature chamber. Hence, it was important to estimate the amount of time taken by the samples to reach their thermal equilibrium and the temperature effect on the FBG sensor's readings.

Thermal analysis can be performed under different approaches: experimentally, analytically or numerically. Analytical solutions for conduction heat transfer are available for cases in which the geometry and the boundary conditions are simple. For most cases, however, it is necessary and more practical to use a numerical approach since the geometry and the case loads in real life tend to be more complex. Some numerical methods include: the Finite Difference, the Finite Volume and the Finite Element method [25].

In this case, a numerical approach was chosen for its simplicity, reliability and relative accuracy. A finite element analysis was implemented using the commercially available FE software: AbaqusTM. With the help of this software, it was possible to estimate the temperature distribution on each sample with respect to time.

2.2 Mathematical Model

The first step for any analysis is to identify the physical conditions in which the system is in. Three different samples were used in the experiment, however, measurements relevant to this project were done on only two: Sample A and B, as shown on figure 1.3. The samples were first at a room temperature of 31 ± 0.5 °C and then placed inside the temperature chamber which was kept at 60 ± 2 °C

[12]. Measurements were taken for sample A in dry conditions inside the chamber, and another set of measurements were performed with both samples in wet conditions. Thus, the mathematical model for the analysis involves heat convection between water or air and the corresponding sample, and heat conduction within the sample.

The basic general energy balance is [26]:

$$\int_V \rho \dot{U} dV = \int_S q dS + \int_V r dV \quad (2.1)$$

where V is the volume of the solid material, with surface area S ; ρ is the density of the material; \dot{U} is the material time rate of the internal energy; q is the heat flux per unit area of the body; and r is the heat supplied internally into the body per unit volume. It is assumed that $U = U(\theta)$, where θ is the temperature of the material.

$$c(\theta) = \frac{dU}{d\theta} \quad (2.2)$$

Heat conduction in a body is governed by the Fourier law,

$$f = -k \frac{\partial \theta}{\partial x} \quad (2.3)$$

where k is the conductivity matrix, $k = k(\theta)$; f is the heat flux; and x is the position. If the material is isotropic then $k = k \cdot I$, where I is the identity matrix.

Heat transfer by convection is described by Newton's cooling law, equation 2.4, where h is the convection coefficient and θ^0 is the sink temperature.

$$q = h(\theta - \theta^0) \quad (2.4)$$

Considering equations 2.3 and 2.4; and since there is no internal heat generation, the energy balance for the present problem is given in equation 2.5

$$\int_V \rho \dot{U} dV + \int_V k \frac{\partial \theta}{\partial x} dV = \int_S h(\theta - \theta^0) dS \quad (2.5)$$

AbaqusTM employs the Galerkin method to solve heat transfer problems [27]. Therefore, by applying it to equation 2.5, it becomes,

$$\delta \theta^N \left\{ \int_V \rho \dot{U} N^N dV + \int_V \frac{\partial N^N}{\partial x} k \frac{\partial \theta}{\partial x} dV - \int_S N^N h(\theta - \theta^0) dS \right\} = 0 \quad (2.6)$$

With respect to the time integration, the backward difference operator (equation 2.7) is employed by AbaqusTM[27] due to its stability. Plugging equation 2.7 into 2.6 gives rise to equation 2.8. These type of systems are then solved through the modified Newton method by the software.

$$\dot{U}_{t+\Delta t} = \frac{U_{t+\Delta t} - U_t}{\Delta t} \quad (2.7)$$

$$\delta\theta^N \left\{ \int_V \rho(U_{t+\Delta t} - U_t) N^N dV + \int_V \frac{\partial N^N}{\partial x} k \frac{\partial \theta}{\partial x} dV - \int_S N^N h(\theta - \theta^0) dS \right\} = 0 \quad (2.8)$$

2.3 Thermal Simulation

The main focus of the analysis was the adhesive layer where the FBG sensors were embedded. However, since both composites have an active role in the heat transfer process, they were both taken into account on the 3D-model of the sample. This consideration requires more computational time but is preferred since it gives a more accurate representation.

The only difference between Sample A and B is that the adhesive layer in sample A has a thickness of 0.2 mm and sample B has a thickness of 0.4 mm. All other aspects are equal for both specimens. Given the symmetric properties of either one of the samples, it was possible to consider only one fourth of the total size of each, as shown on figure 2.1.

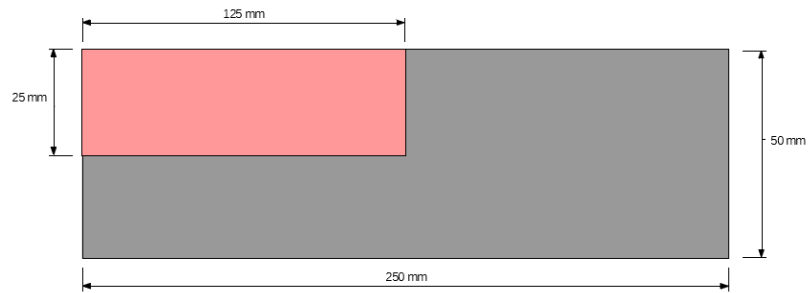


FIGURE 2.1: Section of Sample Considered

Table 2.1 lists the values for the density, thermal conductivity and specific heat used in the simulation, for both, the adhesive and the composite.

TABLE 2.1: Material Properties - Thermal Analysis

Material	Parameter	Value	Units
Adhesive	Density	0.00136	g/mm ³
	Thermal Conductivity	0.000331	W/mmK
	Specific Heat	1.00	J/gK
Composite	Density	0.00187	g/mm ³
	Thermal Conductivity	0.00035	W/mmK
	Specific Heat	1.17	J/gK

The adhesive used was Loctite EA 9394 Aero (a.k.a. Hysol EA 9394), the density and thermal conductivity were given by the manufacturer [24]. It was assumed that the adhesive behaves isotropically. Its specific heat was taken from Lai et al.'s article [28] in which a similar epoxy was employed. The Glass Fiber Reinforced Polymer (GFRP) composites were considered as homogeneous, isotropic materials with properties assumed similar as those stated by Keller et al. [29] and Bai et al.[30] in their works.

Three simulations were carried out. One simulation for when sample A is introduced in the temperature chamber in dry conditions. The second and third correspond to when each sample is submerged in water, respectively. In all cases, there's heat transfer through natural convection with laminar flow. The corresponding convective heat transfer coefficients for air and water were calculated using the correlation equation for natural convection on a flat plate shown on equation 2.9 [31, 32], where Nu, Gr, Pr and Ra stand for Nusselt, Grashof, Prandtl and Rayleigh numbers respectively.

$$Nu = C(Gr \cdot Pr)^n = 0.54Ra^{\frac{1}{4}}$$

$$\frac{h \cdot L}{k} = 0.54 \left(\frac{\rho^2 g_c \beta \Delta T L^3}{\mu^2} \cdot \frac{\mu c_P}{k} \right)^{\frac{1}{4}} \quad (2.9)$$

The meaning of each parameter and its corresponding value for each case is listed on Table 2.2. Properties for both water and air were taken at the average temperature value, $T = (T_f + T_p)/2$, from [33, 34]. The characteristic length for a horizontal plate is defined as $L = \text{surface area}/\text{perimeter}$ [35].

TABLE 2.2: Parameters for Equation 2.9

Symbol	Parameter	Air	Water	Units
ρ	Density	1.109E00	9.901E02	kg/m ³
c_p	Specific heat constant pressure	1.007E03	4.181E03	J/(kgK)
k	Thermal conductivity	2.699E-02	6.370E-01	W/mK
μ	Dynamic viscosity	1.941E-05	5.960E-04	Pa s
β	Coefficient of thermal expansion	3.200E-03	4.150E-04	1/K
g	Gravitational acceleration		9.81	m/s ²
L	Characteristic Length		10,42	m
T_f	Temperature of fluid		333,25	K
T_p	Temperature of plate		304,15	K
ΔT	Temperature difference		29.1	K

With the parameter values and equation 2.9, the heat convection coefficients were estimated to be 4.93 and 819 W/Km² for air and water, respectively. These values are within the expected ranges for natural convection in gases (5 - 30 W/Km²) and in liquids (20 - 1000 W/Km²) [32].

The convection boundary conditions were imposed in the model through a surface film condition interaction only on the top surfaces and external faces. The bottom was considered as insulated since it's in direct contact with the floor of the chamber, and the remaining faces are omitted because of symmetry properties. A tie condition was also used between the adhesive and the composites as it was assumed that there is no thermal resistance between both materials. The tie condition equates temperatures at the matching nodes.

The model was meshed using elements with an approximate global size of 1, and a constraint was placed to have three elements across the thickness of the adhesive. The geometry of the sample enabled the use of 20-node quadratic heat transfer bricks (DC3D20) as elements. Figure 2.2 depicts the mesh on the adhesive as well as the composites. Overall, a total of 15 625 elements and 93788 nodes were employed.

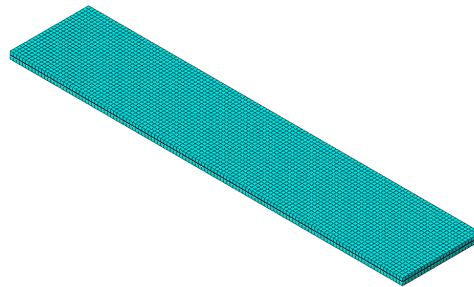


FIGURE 2.2: Refined mesh on model

2.3.1 Simulation - Dry Conditions

In the course of the experiment, measurements with sample A in dry conditions were gathered as a way to study the temperature influence on the FBG sensors and determine the volumetric expansion coefficient as described on equation 1.13. Figure 2.3 shows the temperature distribution on the sample under these conditions.

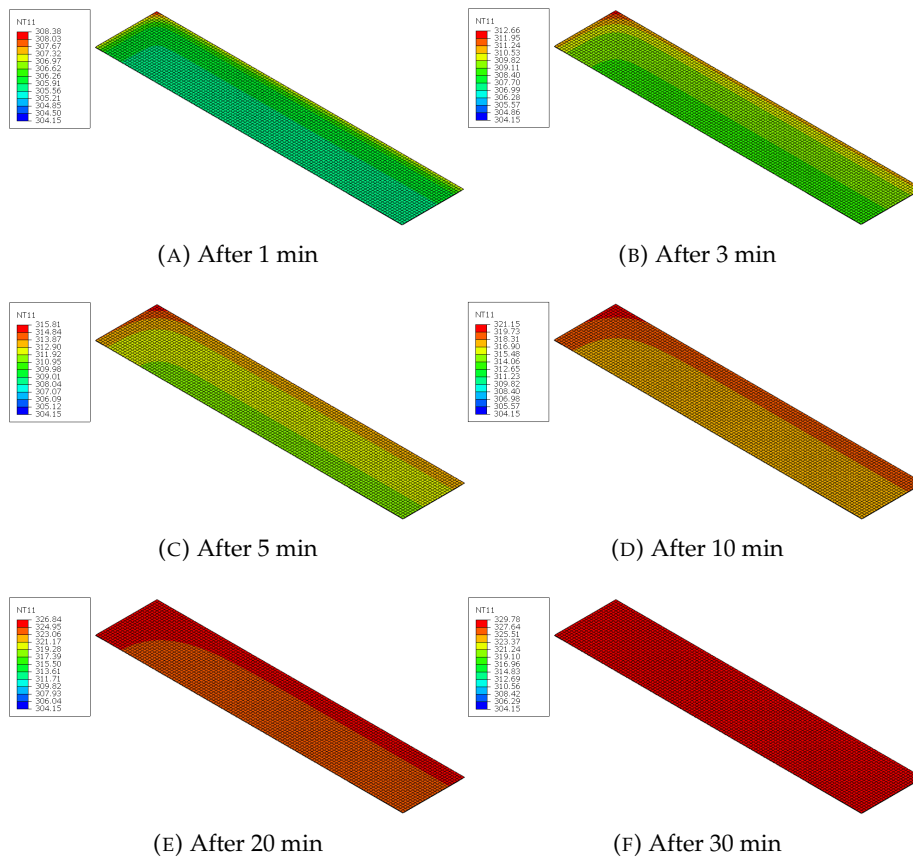
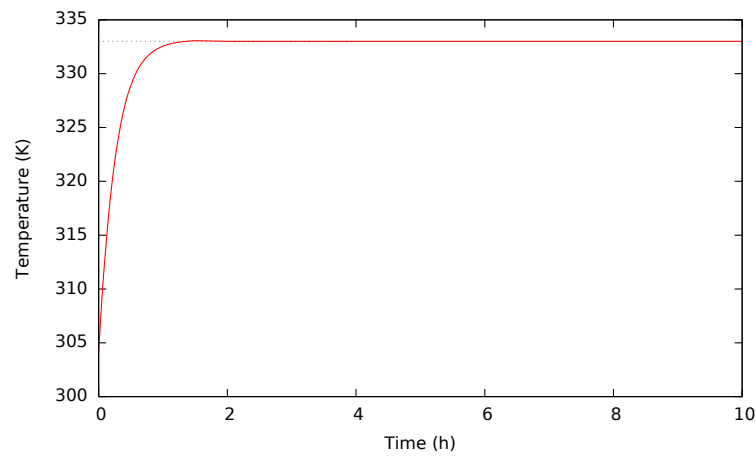
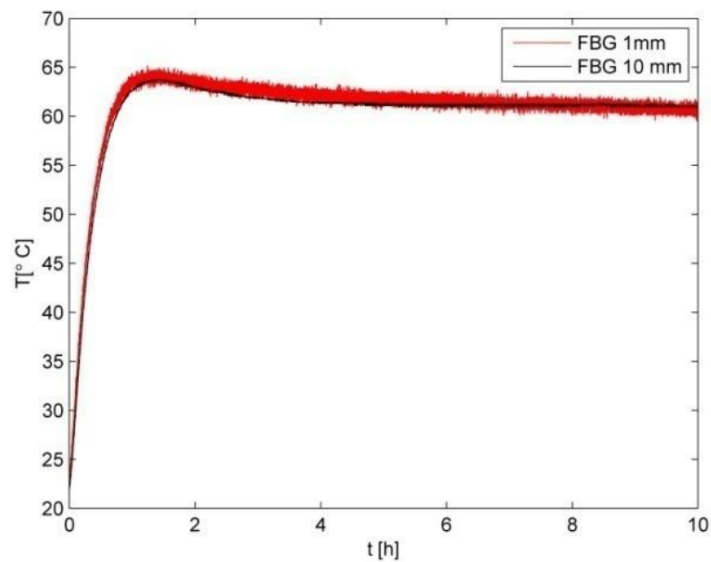


FIGURE 2.3: Sample A - Dry Conditions

The temperature profile for the sample was obtained by monitoring the temperature of a node during the simulation. This node was located in the area where the FBG sensors were placed in the actual sample. Figure 2.4 shows: (a) the temperature profile obtained by the simulation, and (b) the actual measurements, for comparison. The higher curve at the beginning of the experimental results is due to the fact that the temperature chamber needs to go to a higher temperature than the input setting before it can stabilize at the correct temperature.



(A) Simulation Results



(B) Experimental Results [12]

FIGURE 2.4: Temperature Profiles

2.3.2 Simulation - Wet Conditions

Figure 2.5 shows the temperature distribution of sample A and B at different times when in wet conditions. As was expected, the surfaces of the adhesive that are in contact with the water display a higher temperature during the first moments of the simulation. The temperature of the sample continues to rise until it finally reaches thermal equilibrium, an average temperature of 333.15 K, around 5 min after being exposed to the liquid.

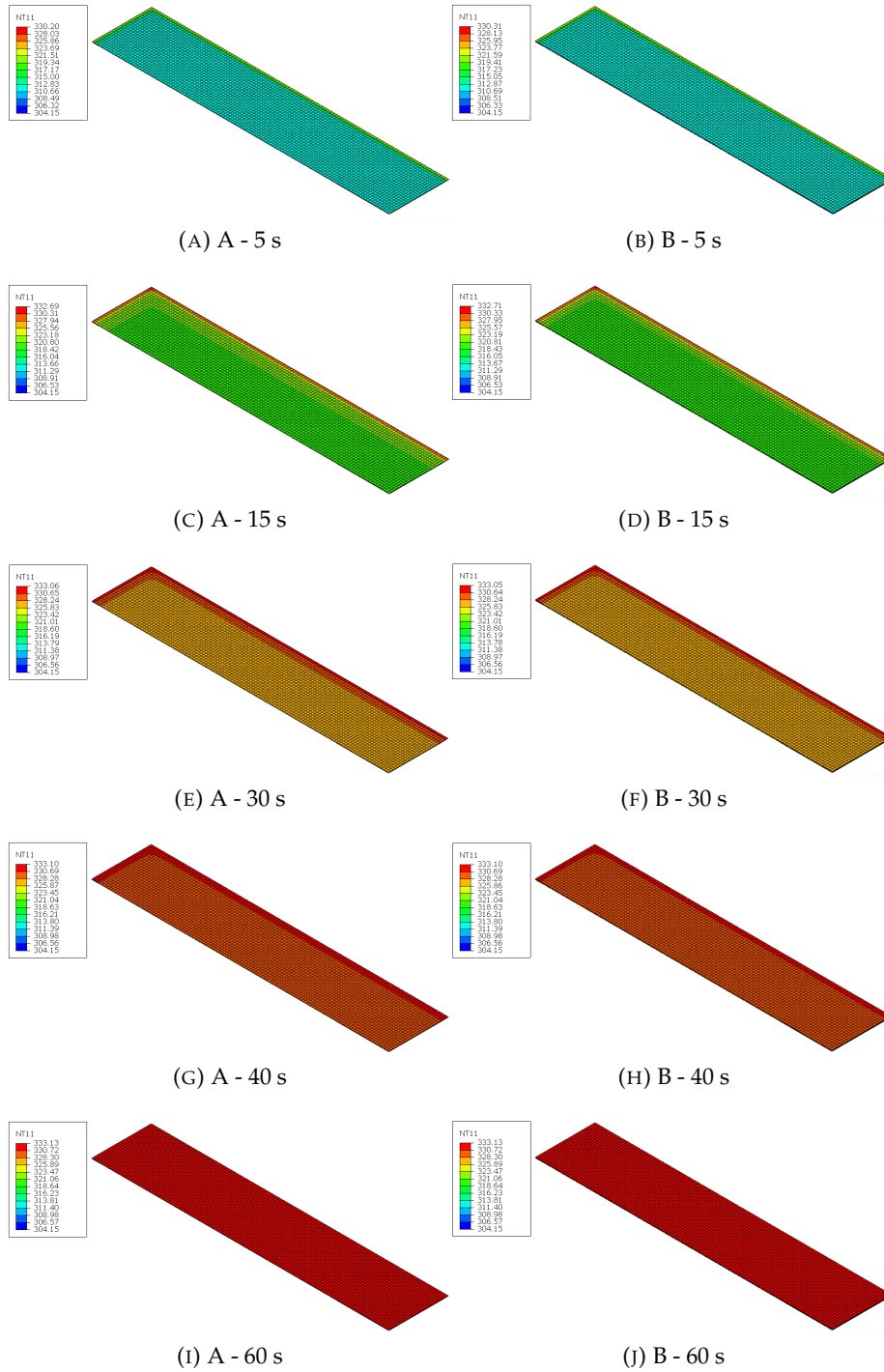


FIGURE 2.5: Sample A and B - Wet Conditions

Graphically, the temperature profile of both samples can be seen on figure 2.6. The chart was created by monitoring a node in the center of the adhesive throughout the simulations. From figure 2.6, one can see that sample B takes a bit longer to reach an equilibrium state due to its higher thickness than sample A. Nonetheless, both samples are able to reach a temperature of 333 K (60 °C) during the first minutes of the experiment.

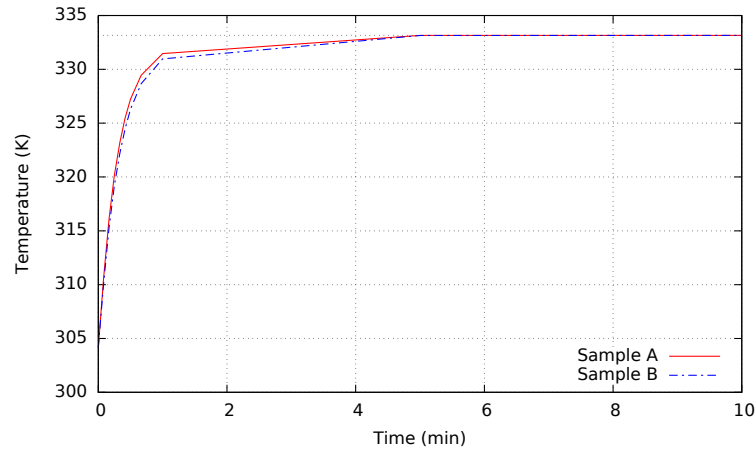


FIGURE 2.6: Sample A and B Temperature Comparison

2.4 Conclusions

The main objective of the thermal analysis was to determine the time it took for the sample to achieve thermal equilibrium in the case in which the sample was placed dry inside the temperature chamber, as well for when the sample was immersed in water.

The main mechanisms for heat transfer in the system were convection between the sample and the fluid, and conduction through the composites and adhesives in the sample. The effects of radiation were assumed to be minimal and thus, neglected. The heat convection coefficients were calculated through a correlation formula for a horizontal flat plate (equation 2.9). In the case of air, the coefficient had a calculated value of 4.93 W/Km^2 . This value is just a little below the lower limit of the typical range for gases which is between 5 and 30 W/Km^2 , but was considered acceptable. For water, the calculated coefficient was 819 W/Km^2 , well between the typical range of 20 - 1000 W/Km^2 .

While in dry conditions, the sample reached thermal equilibrium within the first 40 min, as seen on figure 2.3. A temperature profile was created by monitoring a node in the area where the FBG sensors were located. The simulation results were very similar to the experimental values (figure 2.4). Profiles differ only during the first couple of hours where the experimental values show a temperature spike. This behaviour is due to the temperature chamber which has to induce a higher temperature to be able to stabilise at the desired input setting.

The simulations for the wet conditions, show that samples A and B are able to reach thermal equilibrium during the first 60 seconds (figure 2.5), much more faster than in air. This is not surprising given the magnitude difference between the calculated convection coefficients. Samples A and B were constructed equally, the only difference is that sample B has double the thickness of A. The extra material causes B to take a bit longer to reach thermal equilibrium. Nonetheless, the difference is negligible and by the first 5 minutes both samples reach thermal equilibrium.

Given both samples' temperature profiles when underwater, it is possible to correctly assume both samples in isothermal states during the first sensor measurement, which was done after 6 hours of immersion; and all other measurements, which were done with hour-differences from each other.

Chapter 3

Mass Diffusion Analysis

3.1 Introduction

Many applications have preferred the use of adhesive bonds over traditional mechanical joints due to advantages such as a more homogeneous stress distribution, aesthetic appeal, higher stiffness, high fatigue strength, low weight, the possibility to join dissimilar materials and corrosion prevention [8]. Nonetheless, their use is still limited since many of its properties are negatively affected by environmental conditions.

One of the most important causes for loss of mechanical strength in an adhesive is moisture absorption [28]. By virtue of its polymeric nature, the ingress of water in an epoxy is associated with an increased separation between the molecular chains which cause expansional strains. This phenomenon is referred to as plasticization and it can alter the chemical structure of the component [36]. Studies have shown that moisture intake can be just as damaging as temperature changes in some polymeric structures [37].

The moisture distribution inside an epoxy component is necessary to fully assess the adhesive joint's mechanical response under known environmental conditions. The diffusion characteristics of moisture in an epoxy adhesive are critical factors to predict the moisture profile [11]. Numerical simulations have been successfully used to predict the mass gained by water intake and the mechanisms of diffusion through polymeric materials [38].

In the current project, a diffusion analysis with a finite element model was created to simulate the water ingress inside the epoxy joint of the samples used in the experiment. Two different models for non-Fickian diffusion were used and compared. The progression of the average concentration across the sample with time was calculated and compared to experimental results. The results for the distribution of the water concentration will later be used to quantify the hygro-mechanical behaviour in the following chapter.

3.2 Moisture Diffusion

In his book "The Mathematics of Diffusion", J. Crank defines diffusion as "the process by which matter is transported from one part of a system to another as a result of random molecular motions." [39]. Heat transfer can also be described in the same manner, so it is not surprising that both phenomena are analogous to one another.

Adolf Eugen Fick, was one of the first to make the analogy of diffusion with heat transfer, and in 1855 published his equations. They are now referred to as Fick's first and second law of diffusion.

Fick's first law of diffusion (equation 3.1) describes the overall mass diffusion phenomenon, and it's comparable to the law of heat conduction or Fourier's law (equation 2.3). In it, C is the moisture concentration, J is the mass flux and D is the coefficient of diffusion.

$$\mathbf{J} = -D \cdot \nabla C \quad (3.1)$$

Considering the conservation of mass for the system leads to Fick's second law, also known as the general diffusion law. If one considers uniform diffusivity then equation 3.2 becomes 3.3 [40].

$$\frac{\partial C}{\partial t} = -\nabla \cdot \mathbf{J} \quad (3.2)$$

$$\frac{\partial C}{\partial t} = D \left(\frac{\partial^2 C}{\partial x^2} + \frac{\partial^2 C}{\partial y^2} + \frac{\partial^2 C}{\partial z^2} \right) \quad (3.3)$$

In the case of a one-dimensional diffusion process, i.e. a thin layer of material with a 2h thickness and both surfaces exposed to a constant moisture concentration, C_0 ; the analytical solution for the total moisture is given by equation 3.4 [39]. M_∞ is the amount of solute at saturation.

$$\frac{M(t)}{M_\infty} = 1 - \frac{8}{\pi^2} \sum_{n=0}^{\infty} \frac{1}{(2n+1)^2} \exp \left[-\frac{D(2n+1)^2 \pi^2 t}{4h^2} \right] \quad (3.4)$$

A simple approximation to equation 3.4 is the following [41].

$$\frac{M(t)}{M_\infty} \approx 1 - \exp \left[-7.3 \left(\frac{Dt}{4h^2} \right)^{3/4} \right] \quad (3.5)$$

As can be seen from the previous equations, the diffusivity coefficient, D , and the concentration at saturation, C_{sat} , are important parameters to characterize diffusion in a material. Respectively, they determine the rate of diffusion and the absorption capacity [9]. Both can be obtained by experimental data. In the case of the diffusivity coefficient, it is given by the initial slope when plotting the weight gain, $M(t)$, versus the square root of the time (equation 3.6) [41].

$$D = \pi \left(\frac{2h}{4M_\infty} \right)^2 \left(\frac{M_2 - M_1}{\sqrt{t_2} - \sqrt{t_1}} \right)^2 \quad (3.6)$$

Fick's laws are the basis for understanding diffusion processes in different media. They accurately help quantify the concentration to be expected in many materials. However, it has been noted in multiple studies [36, 42–45] that the majority of polymers show a non-Fickian nature, often named as anomalous diffusion.

Figure 3.1 shows schematic curves for non-Fickian weight-gain absorption data in polymers and polymeric composites [36]. Linear Fickian diffusion is designated by the solid line "LF". Several models have been proposed for the study of diffusion in polymeric materials. Two different models were used and compared in this project: the Time-Varying Boundary Conditions and the Dual-Stage model.

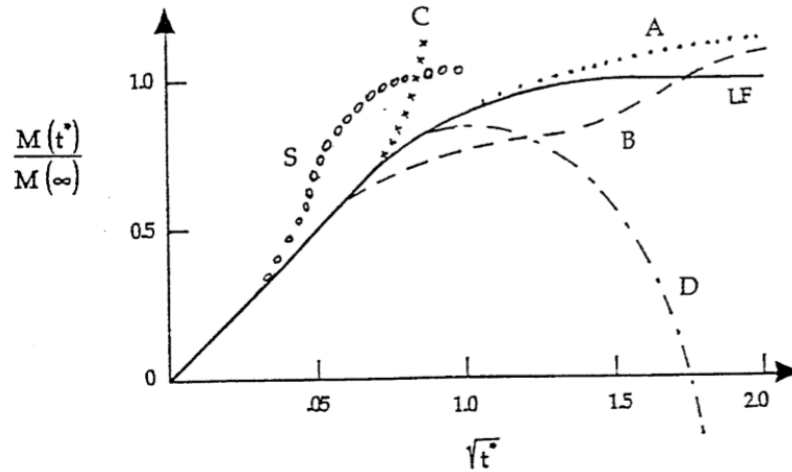


FIGURE 3.1: Schematic curves non-Fickian diffusion in polymers [36]

3.2.1 Time-Varying Boundary Conditions

The viscoelastic nature of polymers can affect the diffusion process by increasing the concentration of moisture at the exposed surfaces of the material with time [44]. In order to take into account this viscoelastic effect, Weitsman and Cai [46] introduced a model with time-varying boundary conditions using Prony series (equation 3.7). C_i and C_r are Prony coefficients, while τ_r is the r th time constant controlling how the concentration is allowed to vary at the boundaries [44].

$$C_0(t) = C_i + \sum_r C_r [1 - \exp(-t/\tau_r)] \quad (3.7)$$

Considering the one-dimensional case of equation 3.3, with an initial concentration, $C(x, 0) = 0$, and boundary conditions equal to equation 3.7 with $C_i = 0$ and one exponential term; the solution is given by equations 3.8 and 3.9 [39]. Both equations will be denoted by \hat{C} and \hat{M} , respectively, for future reference.

$$\begin{aligned} \frac{\hat{C}(x, t)}{C_\infty} = & 1 - \exp(-\beta t) \frac{\cos[x(\beta/D)^{0.5}]}{\cos[h(\beta/D)^{0.5}]} \dots \\ & - \frac{16\beta h^2}{\pi} \sum_{n=0}^{\infty} \frac{(-1)^n}{2n+1} \frac{\exp[-D(2n+1)^2\pi^2 t/4h^2]}{[4\beta h^2 - D\pi^2(2n+1)^2]} \cos \frac{(2n+1)\pi x}{2h} \end{aligned} \quad (3.8)$$

$$\begin{aligned} \frac{\hat{M}(t)}{M_\infty} = & 1 - [\exp(-\beta t)(D/\beta h^2)^{0.5} \tan(\beta h^2/D)^{0.5} \dots \\ & - \frac{8}{\pi^2} \sum_{n=0}^{\infty} \frac{1}{(2n+1)^2} \frac{\exp[-D(2n+1)^2\pi^2 t/(4h^2)]}{1 - (2n+1)^2 [D\pi^2/(4\beta h^2)]}] \end{aligned} \quad (3.9)$$

For the general case with time-varying conditions, the solution is given by a linear combination of \hat{C} , \hat{M} , C_H and M_H , as can be seen on equations 3.10 and 3.11 [46]. The last two terms correspond to the solution of the one-dimensional Fick equation with an initial condition of zero and uniform boundary concentrations equal to one. Both are given in equations 3.12 and 3.13 [39]. The variables C_0 , C_∞ and M_∞ stand for the concentration at the boundary, concentration at saturation and total amount of solute at saturation, respectively.

$$\frac{C(x, t)}{C_\infty} = \frac{C_i C_H(x, t)}{C_\infty} + \sum_{r=1}^R \frac{C_r}{C_\infty} \hat{C}(x, t; \beta_r) \quad (3.10)$$

$$\frac{M(t)}{M_\infty} = \frac{C_i}{C_\infty} M_H(t) + \sum_{r=1}^R \frac{C_r}{C_\infty} \hat{M}(t; \beta_r) \quad (3.11)$$

$$\frac{C_H(x, t)}{C_0} = 1 - \frac{4}{\pi} \sum_{n=0}^{\infty} \frac{(-1)^n}{2n+1} \exp\left[-\frac{D(2n+1)^2 \pi^2 t}{4h^2}\right] \cos\frac{(2n+1)\pi x}{2h} \quad (3.12)$$

$$\frac{M_H(t)}{M_\infty} = 1 - \frac{8}{\pi^2} \sum_{n=0}^{\infty} \frac{1}{(2n+1)^2} \exp\left[-\frac{D(2n+1)^2 \pi^2 t}{4h^2}\right] \quad (3.13)$$

Experimental results can be used to obtain the parameters used on equation 3.13. Keep in mind that $\beta_r = 1/\tau_r$. Weistman and Cai [46] give a detailed account on how to go about this particular fitting. In their investigation, LaPlante et. al. [44] concluded that the time-varying model with one exponential term was the model that showed a better approximation to their experimental results when compared to other models.

3.2.2 Dual-Stage Model

Non-Fickian behaviour is observed in polymers when their temperature is less than the glass transition temperature (T_g), as it is in this case. This anomalous behaviour could be the consequence of the relaxation process and/or chemical interaction between the water molecules and the polymer chains [47]. Under the glass transition temperature, many properties of polymers are time-dependent, e.g. the stress may be slow to decay after the polymer has been stretched [39]. Anomalous diffusion occurs when the diffusion and relaxation rates are comparable, i.e. the polymer chains don't adjust as quickly to the presence of the penetrant.

The dual-stage model is characterized by the schematic curve labelled as "B" on figure 3.1. Some studies have been able to model this behaviour by the use of two parallel Fickian processes, others have used two sequential Fickian processes instead. For their study, Shirangi and Michel [48] compared both approaches and found that the two sequential Fickian processes adapted better to experimental data. As such, this approach was chosen for the current project.

The main parameters of the dual-stage model are: diffusion coefficients for the first and second stage, D_1 D_2 , concentrations of saturation at the first and second stage, $M_{\text{inf } 1}$ $M_{\text{inf } 2}$ and the time at which the change is made. All of this

information can be obtained from the experimental data directly and by using equation 3.6 for the diffusivity coefficients.

3.3 Weak form discretization

The diffusion analysis was made through the mass diffusion analysis options in Abaqus/CAE. On the grounds of mass conservation, the diffusion analysis is stated in equation 3.14. In it, V is the volume with surface S , n is the outward normal to S , J is the flux of concentration of the diffusing phase, and $n \cdot J$ is the concentration flux leaving S [49].

$$\int_V \frac{dC}{dt} dV + \int_S n \cdot J dS = 0 \quad (3.14)$$

Applying the divergence theorem, it can be simplified to,

$$\int_V \left(\frac{dC}{dt} + \frac{\partial}{\partial x} \cdot J \right) dV = 0 \quad (3.15)$$

To be able to handle cases between dissimilar materials, Abaqus takes the normalized concentration, ϕ , as the solution variable. The normalized concentration is defined in equation 3.16, where C is the concentration of the diffusing material and s stands for the solubility in the base material [49].

$$\phi = \frac{C}{s} \quad (3.16)$$

The flux of concentration, J , is defined according to Fick's law (equation 3.3), which is slightly modified to accommodate the use of the normalized concentration. In equation 3.17, D stands for the diffusivity coefficient.

$$J = -D \cdot \left(s \frac{\partial \phi}{\partial x} + \phi \frac{\partial s}{\partial x} \right) \quad (3.17)$$

In this project, solubility is assumed to remain constant. Hence, equation 3.17 is simplified to equation 3.18.

$$J = -sD \cdot \frac{\partial \phi}{\partial x} \quad (3.18)$$

Applying the variational principle to equation 3.14 and considering J as given by equation 3.18, the weak form of the diffusion problem is obtained (equation 3.19) [50].

$$\int_V \left[\delta\phi \left(s \frac{d\phi}{dt} \right) + \frac{\partial \delta\phi}{\partial x} \cdot sD \cdot \frac{\partial \phi}{\partial x} \right] dV = \int_S \delta\phi - n \cdot \left(-sD \cdot \frac{\partial \phi}{\partial x} \right) dS \quad (3.19)$$

The variable $\delta\phi$ is an arbitrary, scalar field as per the variational principle. Abaqus considers the Galerkin method, therefore $\delta\phi$ is defined as equation 3.20, where N^N are the interpolation functions [50].

$$\delta\phi = N^N \delta\phi^N \quad (3.20)$$

For transient analysis, like in this project, the backward Euler scheme is used for the time integration. Therefore, the discretize version of equation 3.19 is as follows [50],

$$\int_V \left[N^N \left(s \frac{d\phi}{dt} \right) + \frac{\partial N^N}{\partial x} \cdot sD \cdot \left(\frac{\partial \phi}{\partial x} \right) \right] dV = \int_S N^N n \cdot \left(-sD \cdot \frac{\partial \phi}{\partial x} \right) dS \quad (3.21)$$

3.4 Diffusion Model

As in the thermal analysis, the geometric and loading symmetries allow the use of just one part of the model for the diffusion analysis. In this case, one fourth of the model was considered. The main focus of the analysis was the evolution of the moisture distribution within the adhesive with time. Two different models were used for this purpose: Time-Varying Boundary Conditions and Dual-Stage.

3.4.1 Material Properties

Time-Varying Boundary Conditions

The material properties considered for the analysis are given on table 3.1. The density is given by the manufacturer [24]. The diffusion coefficient was determined by conducting a linear fit on the first four points of the experimental data and using equation 3.6. The experimental data corresponds to sample A only, hence the thickness to be considered is 0.2 mm.

Solubility is defined as the concentration at saturation, which is the maximum amount of a substance that can be dissolved per the amount of a solvent [3]. Abaqus uses solubility to calculate the normalized concentration (equation 3.16), and all boundary conditions must be given as normalized concentrations as well. This means that if a surface is in full contact with the penetrant a boundary condition equal to one should be applied. In this project, due to the nature of the boundary conditions used, it was preferable to choose a solubility of 1 and boundary concentrations as concentration at saturation when necessary.

TABLE 3.1: Material Properties - Time-Varying BC

Parameter	Value	Units
Density	0.00136	g/mm^3
Diffusion	0.00018325	mm^2/h
Solubility	1.00	

Dual-Stage

At first glance, the weight-gain data for sample A (figure 1.4) might not give the impression of a dual stage diffusion. However, by taking a closer look, it is possible to distinguish two stages with different saturation points. Both of these stages are pointed out on figure 3.2, where the first three points of the experimental data were omitted.

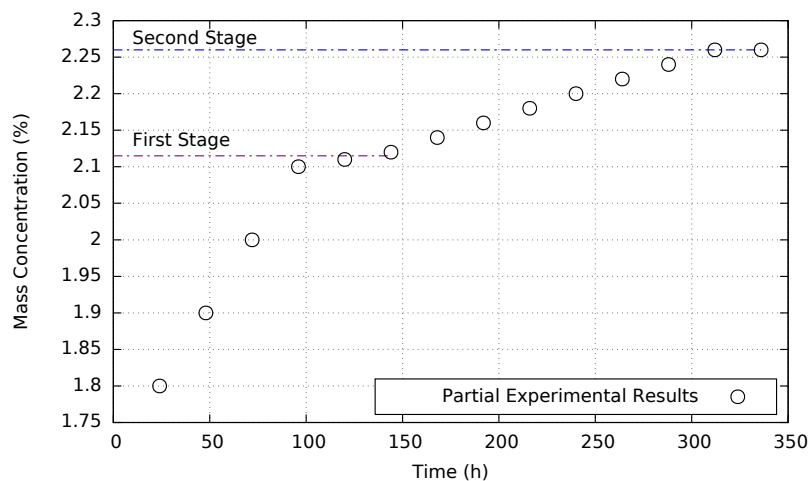


FIGURE 3.2: Dual-Stage on Experimental Data

The mass saturation concentrations for each stage are 0.0211 and 0.0226, respectively. The corresponding diffusion coefficients were calculated by equation 3.6, doing a linear fit on each of the two slopes. It's important to note that for the second stage, the concentration used in the equation is 0.0015, the difference between both saturation concentrations.

In order to allow the change of diffusion properties in the model, it was necessary to create a time dependency in Abaqus. To do so, the diffusion coefficients were defined as dependant to a field variable; and then this field variable was defined equal to the total time of the simulation. This was done through user subroutine UFIELD. Appendix A shows the respective Fortran code. The time chosen for the change of properties was 140 hours.

As for the solubility, it was preferred to keep it as unity and account for the different saturation concentrations through the boundary conditions. Table 3.2 lists the material properties for this analysis.

TABLE 3.2: Material Properties - Dual Stage

Parameter		Value	Units
Density		0.00136	g/mm ³
Diffusivity	1st Stage (0-140h)	0.00021023	mm ² /h
	2nd Stage (140-336h)	0.00022764	mm ² /h
Solubility		1.00	

3.4.2 Boundary Conditions

Time-Varying Boundary Conditions

Given the fact that the adhesive is a polymeric material, it was clear that it would not follow a Fickian diffusion. To take into account the non-Fickian nature of the adhesive, the time-varying boundary conditions model was used (section 3.2.1). Thus, all the surfaces of the adhesive in contact with water were given boundary conditions following equation 3.7.

Abaqus allows the definition of an amplitude function to be applied with its loads and boundary conditions. This amplitude can be chosen from a list of in-built functions or it can be user-defined through a user subroutine. In this case, the in-built function for exponential decay (equation 3.22) was chosen since, with just minor adjustments of constants, it equals the desired boundary

condition. Table 3.3 shows the relations between the parameters from both equations and the values used for the different values of diffusion mentioned earlier. Parameter values were chosen to best fit the experimental data.

$$a = A_0 + A \exp(-(t - t_0)/t_d) \quad (3.22)$$

TABLE 3.3: Boundary Condition Parameters

Decay Parameters	Equation 3.7 Parameters	Values Used
A_0	$C_i + C_1$	0.037
A	$-C_1$	-0.0075
t_d	τ	1250
t_0	0	0

Dual-Stage Model

For the case of the dual-stage model, since solubility was defined equal to one, the boundary conditions for the adhesive had to be equal to the two saturation concentrations discussed in section 3.4.1. The boundary conditions for the first stage remain constant up to the time break when the second stage begins. As mentioned, Abaqus is able to apply an amplitude with its boundary conditions so they can be altered with time. In this case a tabular amplitude was used to resemble a step function for the saturation concentrations.

At first, the composites were considered to be an impermeable barrier for the adhesive and as such only the external faces of the adhesive were considered as areas of water ingress. This assumption was supported by weight-gain data for the composite that showed that after one month it could only retain 1.96% of water moisture. Yet, the simulation results, shown on figure 3.3, proved that if only those faces were considered, the saturation concentration could not be reached during the first 50 hours.

After a second look at the composite-adhesive interface, it is very likely that water could make direct contact through the top and bottom faces due to the roughness and porosity of the composite. This assumption was later corroborated by the simulation results. Therefore, the top and bottom surfaces were applied time-varying and saturated boundary conditions as well.

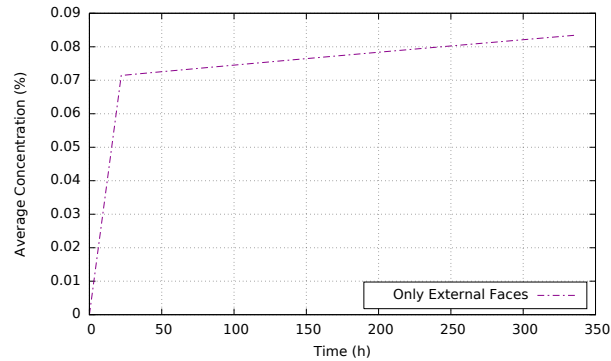


FIGURE 3.3: Diffusion Analysis - Only External Faces

3.4.3 Model Mesh

One of the main goals of the mass diffusion analysis was to use the concentration results in the following mechanical analysis. To be able to import the results properly it was necessary for both, the mass diffusion and the mechanical analyses, to have the exact same mesh. In the mechanical analysis, the main areas of interest were the locations of the FBG sensors to compare the measurements with the simulation results. Hence, it was necessary to have elements at the center of the adhesive. With this in mind, a constraint was placed on the thickness of both sample models so that there would be three elements through it. As for the rest of the sample a uniform mesh was chosen.

Mass diffusion analyses can be performed using only the two-dimensional, three-dimensional, and axisymmetric solid elements that are included in the Abaqus/Standard heat transfer/mass diffusion element library [49]. The type of elements chosen were first-order brick elements (type DC3D8). At first a global size mesh of 1 mm was used, but then it was refined to a 0.5 mm mesh to improve the aspect ratio of the elements. Results with both meshes were compared. In total, with the 1 mm mesh, 9375 elements (13104 nodes) were used; with the 0.5 mm mesh the number increased to 37 500 elements (51 204 nodes). Figure 3.4 shows a detail of both meshes.

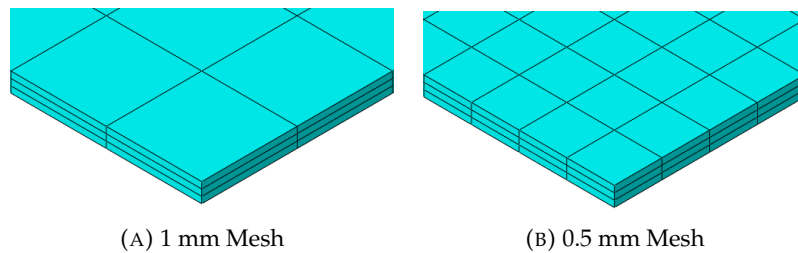


FIGURE 3.4: Sample mesh

3.5 Results

The experimental data was given as a percentage of weight gain, $M(t)$. However, the analysis is ran using average concentration, $C(t)$, as the main variable. To be able to compare the simulation results with the experimental data, the weight-gain data was converted to average concentration. The average concentration was calculated through equation 3.23 [28, 51], where $\rho_{epoxy} = 0.00136$, g/mm^3 [24] and $\rho_{water} = 0.0009832$ g/mm^3 [33] are the densities of the epoxy and water at $60^\circ C$, respectively. The experimental results for average concentration are shown on figure 3.5, where one can see that the concentration at saturation is 3.126%.

$$C(t) = \frac{\rho_{epoxy}}{\rho_{water}} M(t) \quad (3.23)$$

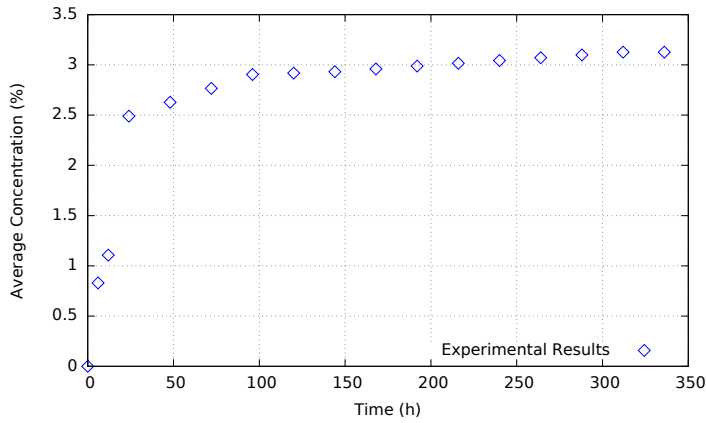


FIGURE 3.5: Average Concentration - Experimental results

The finite element model calculates the concentration percentage at each integration point. Thus, to compare results, the average concentration of the whole sample at each time increment was calculated using equation 3.24 [52]. C_i and V_i stand for the concentration and the volume at the integration point, respectively. The formula was implemented through a simple Python script that reads through the Abaqus results database and extracts the pertinent information. An example of such a script is presented in Appendix B.

$$C_{ave} = \frac{\sum_{i=1}^n C_i V_i}{\sum_{i=1}^n V_i} \quad (3.24)$$

3.5.1 Average Concentration - Whole Sample

Two different approaches for the modelling of the concentration distribution across the samples were used: the Time-Varying Boundary Condition and the Dual-Stage model. The weight-gain experimental data is given for Sample A only. The average concentration from the FEA results was calculated with equation 3.24. Figure 3.6 shows the comparison between the experimental measurements and the results for both models.

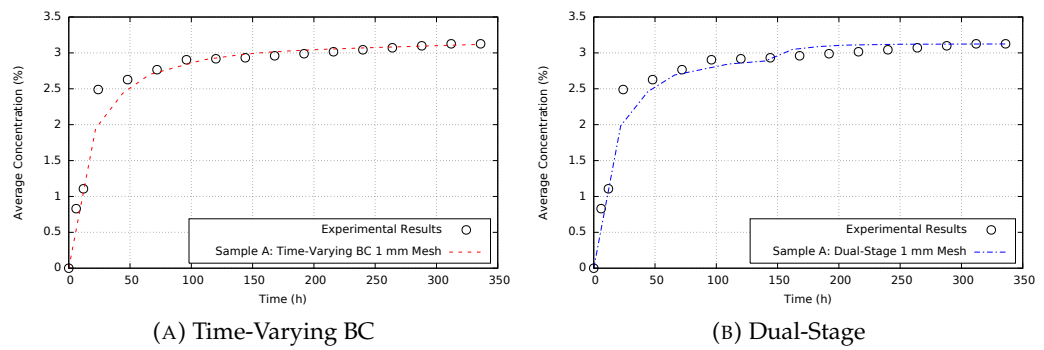


FIGURE 3.6: Average Concentration - Whole Sample

Since the adhesive is below its glass transition temperature, it shows a non-Fickian behaviour. This behaviour is taken into account by both of the models used. Had this not been the case, the model would have followed a Fickian profile. For comparison, figure 3.7 shows the average concentrations obtained by the models and the analytical solution for Fickian diffusion.

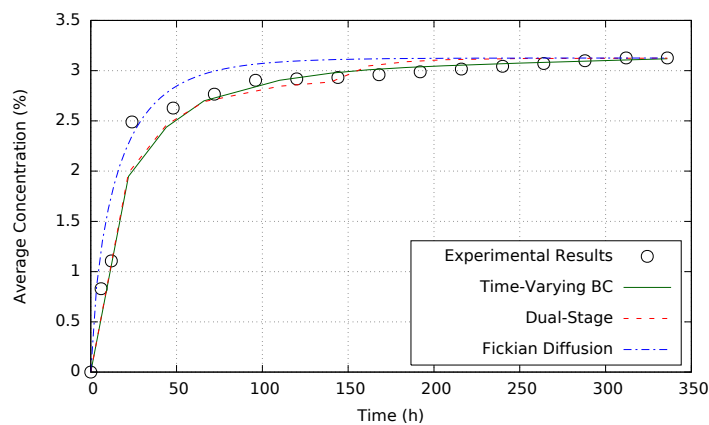


FIGURE 3.7: Comparison Fickian Profile

3.5.2 1 mm vs 0.5 mm Mesh

Two different meshes were used for the simulations; a uniform mesh with a global element size of 1 and a more refined mesh with a global element size of 0.5. Usually, the use of more and finer elements leads to a more precise result at the cost of more computational time. The concentration profiles obtained from simulations with each mesh and with each model are compared in figure 3.8.

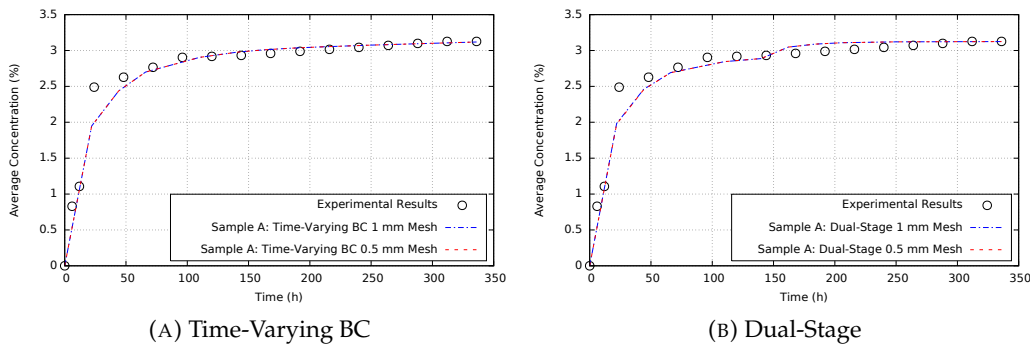


FIGURE 3.8: Mesh Comparison

In both cases, it is clear that the use of the 1 mm mesh is sufficient enough to get a reliable concentration profile. A refined mesh is not necessary since the desired result is not focused on a particular section of the adhesive but rather the average concentration across the whole sample. For the subsequent mechanical analysis, however, results are wanted from specific areas of the sample where a more refined mesh might prove more accurate. The difference in computational time between each mesh for each case is presented in table 3.4.

TABLE 3.4: Computational Times per Mesh Size

	Sample A		Sample B	
	1 mm	0.5 mm	1 mm	0.5 mm
Time-Varying	15 s	44 s	18 s	55 s
Dual-Stage	17 s	47 s	16 s	48 s
Problem Size	9 375 elem. (13 104 n.)	37 500 elem. (51 204 n.)	9 375 elem. (13 104 n.)	37 500 elem. (51 204 n.)

3.5.3 Average Concentration - Sample A and B

For the experimental results, two samples were used: sample A and sample B. Both samples were put under the same environmental conditions. The only difference between the samples is the adhesive thickness; sample A has a thickness of 0.2 mm while sample B has a bigger thickness of 0.4 mm. Simulations were ran for both samples. Figure 3.9 shows the average concentration profiles of each sample per modelling approach.

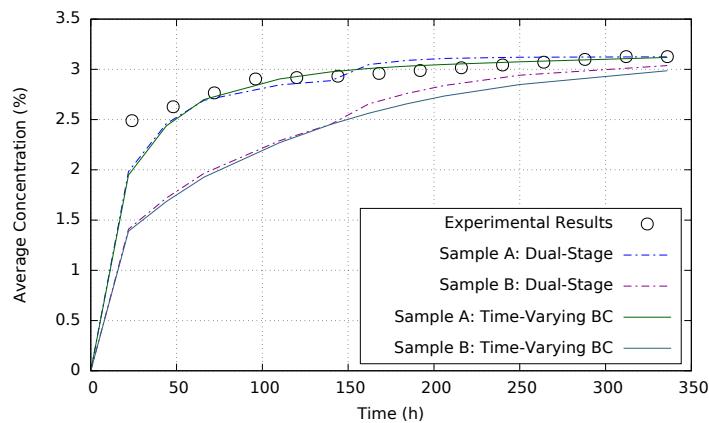


FIGURE 3.9: Average Concentration - Sample Comparison

The concentration profiles for both samples differ greatly between each other. Sample A is able to reach its concentration of saturation much faster than sample B. This is not surprising given that sample A has less volume than sample B.

3.5.4 Average Concentration - Sensor Areas

As was mentioned, each sample has FBG sensors embedded in the adhesive layer. Sample A has a 10mm FBG sensor located near the center and Sample B has a 10 mm FBG sensor located more closely to the edge of the sample. In the numerical model, sets of elements were created for the areas where the FBG sensors were located in both of the samples.

A comparison between results for these areas for each sample is shown on figure 3.10. The results show that being closer to the edge or at the center has no impact on the average concentration within the sensor area.

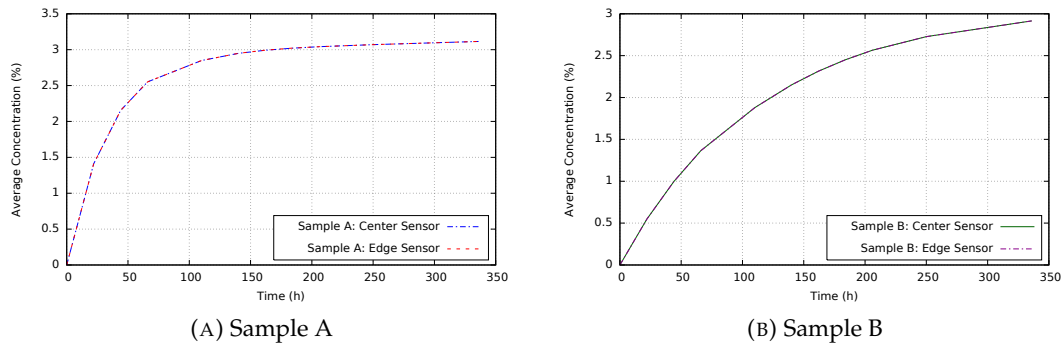


FIGURE 3.10: Sensor Area Comparison

3.5.5 Concentration Distribution

The average concentration of the sample was calculated in order to compare simulation results with the experimental results. Nonetheless, the most important result from the analysis is the concentration distribution on the sample and its progression with time. Figure 3.11 shows the distribution across the thickness of sample A and B.

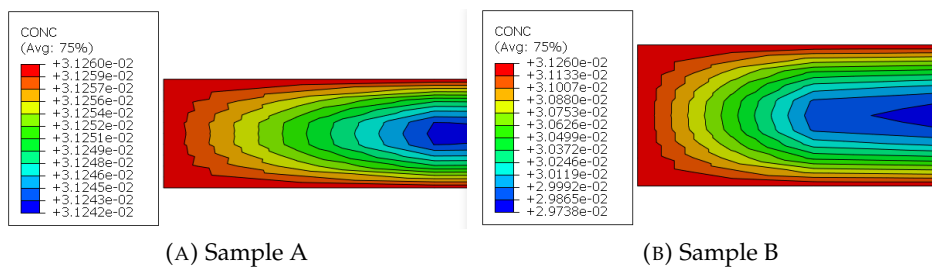


FIGURE 3.11: Concentration Distribution at 336 h

As was expected, areas in contact with water show a higher concentration very early in the simulation. In the case of sample A, the saturation concentration is reached rapidly with only slight differences in the third and fourth decimals of the concentration values. On the other hand, sample B is only able to reach a saturation state towards the end of the simulation.

The concentration progression with time in each sample is depicted on figure 3.12. The limits of each frame were kept the same for a fair comparison. After the 140th hour, for sample A, there are no visible changes across the sample since the concentration differences are minimal.

3.6 Conclusions

A diffusion analysis by means of a finite element model was executed in order to obtain the concentration distribution of the moisture absorbed by the adhesive in sample A and B. This allowed a better understanding of the diffusion process within the material. Comparison with the experimental results was possible by converting the experimental weight-gain data into average concentration [3.23](#) and by calculating the average concentration at the integration points of the whole model with equation [3.24](#).

Several models for non-Fickian diffusion can be found in the literature. In this project, two were chosen: Time-Varying boundary conditions and the Dual-Stage model. The average concentration for each model was compared to the experimental results as is shown on fig [3.6](#). From the two, the time-varying BC shows a good fit with the data. However, this is expected since the parameters in equation [3.10](#) are chosen to provide the best fit.

The parameters for the dual-stage model are the saturation concentrations and the diffusion coefficients at each stage, the latter are calculated theoretically through equation [3.6](#). The Dual-Stage model provides a reasonable fit to the data overall. However, it tends to underestimate the concentration during the first stage and overestimate concentrations for the second stage. This relates directly to the diffusion coefficients and the error when calculating them from very few data points.

In any case, both models account for the viscoelastic nature of the adhesive and how it can slow down the diffusion process. When compared to a completely Fickian diffusion (figure [3.7](#)), it is clear that the Fickian diffusion overestimates the concentration, especially during the first hours of the simulation.

The main drawback of either one of the models used for anomalous diffusion is that the parameters have to be obtained through experimental data which, of course, limits its implementation.

As in any finite element model, the way a continuum is discretize can greatly affect the whole analysis. If a mesh is too course, the results may be unreliable and too fine a mesh may lead to a very high computation cost and a lengthy analysis. During this analysis, two meshes were implemented. The first one was a uniform mesh with a global element size of 1 mm; and a finer mesh with 0.5 elements.

The results obtained, figure [3.8](#), show that the use of the more refined mesh doesn't have an impact on the predicted average concentration values across the whole sample. Nonetheless, it may have an impact when focusing on a smaller area of the sample which is the case for the subsequent mechanical analysis.

Computational times are increased three times when using the finer mesh, but since times are still under a minute it's not considered a limitation. Both meshes were used for the following mechanical analysis and results compared.

Experimental results used two different samples. The samples differ from each other only by their thickness; sample A has an adhesive thickness of 0.2 mm and sample B a 0.4 mm thickness. Models for both samples were created and average concentrations results from both samples are shown on figure 3.9. The results show that the thickness difference has a very strong influence on the concentration across the sample. Clearly, Sample A has less volume and is able to reach a saturated state within the first 140 h. The concentration across sample B is increasing steadily up to the last few hours of the simulation when concentration values differ slightly between each other.

FBG sensors were embedded into the adhesive layer of each of the sample. In sample A, a 10 mm FBG sensor was located at the center and in sample B the sensor was located closer to the edge. It was believed that the sensor located at the edge would be subjected to a higher moisture concentration than the one in the center. As figure 3.10 shows, that is not the case. The amount of moisture entering the sample from the external faces is negligible when compared to the top and bottom faces. Hence, the main contributor for the differences in concentrations between the sensors is not their location but the fact that they are embedded in samples with different thicknesses.

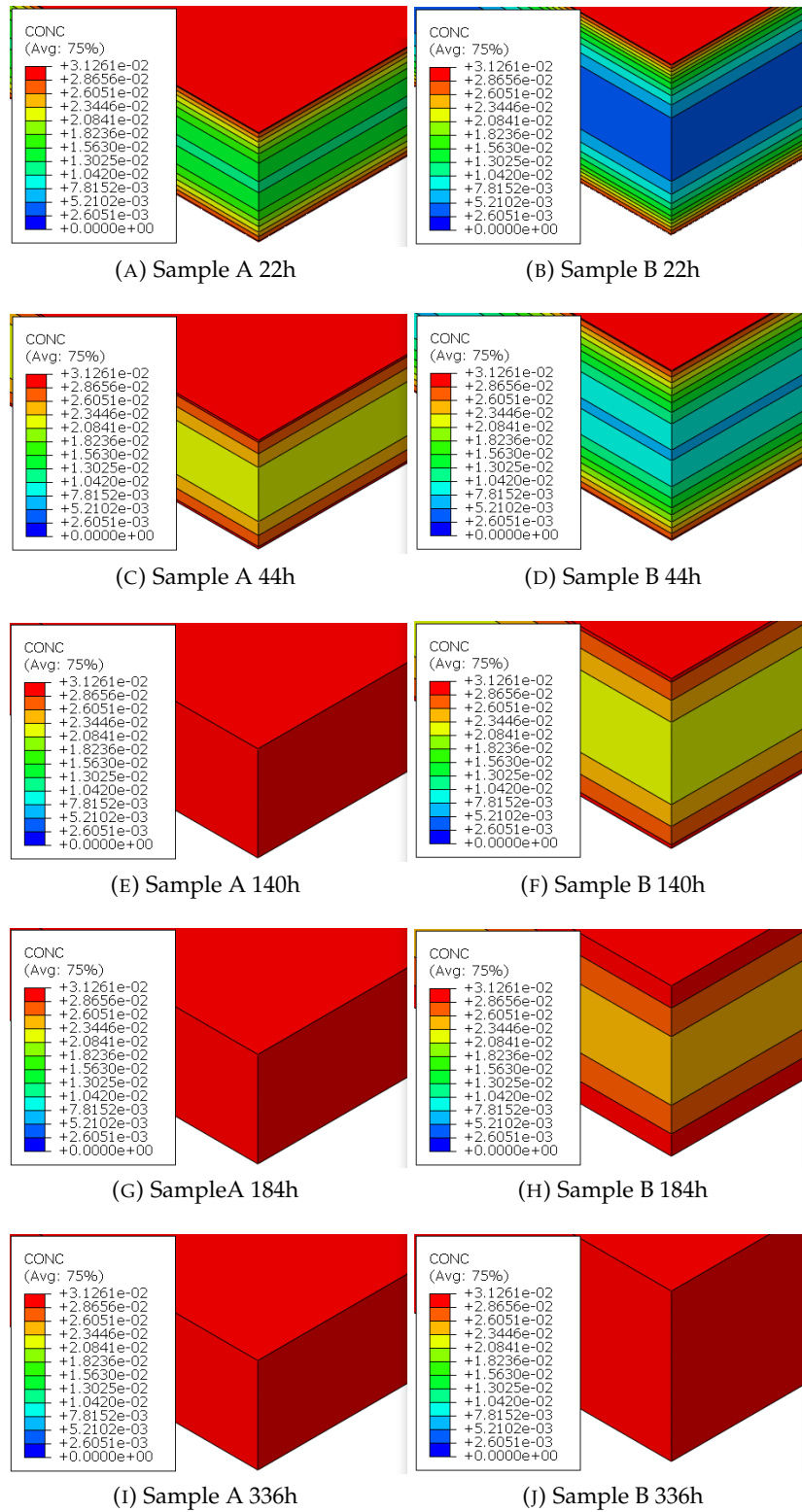


FIGURE 3.12: Concentration Distribution Progression

Chapter 4

Hygro-Mechanical Analysis

4.1 Introduction

The ingress of water molecules into a polymeric material leads to the chemical interaction between the water molecules and the polymer chain. This interaction leads to two different stages of water that can be found in the polymeric material. A percentage of the water molecules group in the voids and cavities within the material, these are referred to as the "free" or "unbounded" molecules. In contrast, the rest of the molecules are called "bounded" since they interact with the polymer chains and form hydrogen bonds [37]. These states have been detected through the use of spectroscopic methods [53, 54].

The absorption of water by an adhesive produces an overall expansion in the material's volume. This behaviour is known as hygroscopic swelling. Studies have observed that the ratio between the hygroscopic swelling volume and the volume of absorbed water is less than one [55, 56]. Hence, not all the absorbed water molecules have an active role in the expansion. It is very likely that only the "bounded" molecules contribute to the expansion. When water molecules form hydrogen bonds with the hydroxyl groups found in polymers, it causes a disruption in the inter-chain hydrogen bonding leading to an increase in the inter-segmental hydrogen bond length [56] which leads to swelling.

The hygroscopic swelling of a polymer can produce hygroscopic stresses if there's a material response mismatch in the structure. These stresses are similar to the stresses caused by thermal expansion [57]. Both effects can add up and affect the total mechanical response of the adhesive joint. Hygroscopic stresses are related to moisture content very similarly to how thermal stresses are related to thermal distributions. The stress distribution caused by hygroscopic swelling has been successfully calculated through the use of finite element techniques [58–62].

In this project a sequentially coupled hygro-mechanical analysis was performed. The concentration profiles calculated in 3, were used in a mechanical analysis in Abaqus. The strain distribution and evolution against time due to moisture concentration was obtained. Results were compared to those obtained by the FBG readings done in the base experiment.

4.2 Hygroscopic and Thermal Strain

The absorption of water by a polymer causes a swelling in the material known as hygroscopic swelling and the deformation of the material referred to as hygroscopic strains. It has been found that hygroscopic strains, ϵ_{hygro} , follow a linear relationship with the change in concentration in the material ΔC . The behaviour is in analogy to how thermal strains, $\epsilon_{thermal}$, linearly depend on the temperature difference, ΔT . Both dependencies are mathematically shown on equations 4.1 and 4.2 [62].

$$\epsilon_{hygro} = \beta \cdot \Delta C \quad (4.1)$$

$$\epsilon_{thermal} = \alpha \cdot \Delta T \quad (4.2)$$

The symbols β and α stand for the coefficients of hygroscopic swelling and thermal expansion, respectively. Both can be determined experimentally. In the case of α , it can be found listed for many materials.

Under normal conditions, a material can be subjected to temperature changes, differences in moisture concentration and mechanical loads. Thus, the total deformation in the material is given by the sum of all three induced strains (equation 4.3 [62]).

$$\epsilon_{total} = \epsilon_{mechanical} + \epsilon_{thermal} + \epsilon_{hygro} \quad (4.3)$$

In this particular experiment, the samples were exposed to thermal and moisture concentrations changes only. As was explained in chapter 1, thermal strains were measured in a separate experiment and hygroscopic strains were calculated through equation 1.14.

This linear superposition of the mentioned strains is applicable when the total resulting stress is below the material's elastic limit [62]. Experimental results show that the strains are small enough so that this is the case at all times.

4.3 Hygro-Mechanical Model

4.3.1 Coupling the Mass Diffusion Analysis

In order to quantify the deformation suffered by the material due to moisture absorption, a mass diffusion analysis was carried out on models for both of the experimental samples (Chapter 3). The spatial moisture concentration profile of each was then sequentially combined with a mechanical deformation analysis. Both analyses were executed through the Abaqus/CAE finite element software.

Abaqus doesn't offer the possibility to directly use the concentration distribution for a hygro-mechanical analysis. It does, however, offer the option to perform a thermo-mechanical analysis. Given the close similarities between both phenomena, it was possible to use this capabilities for the hygro-mechanical analysis.

The normalized concentration values at each node were imported into the mechanical analysis as temperature values. This was achieved through the Fortran code developed by S. Yoon, C. Jang and B. Han [58]. The code is presented on Appendix C. It reads the record key of the mass diffusion results database and changes it from normalized concentration (key 221) to nodal temperature (key 201). Then, the results can be imported into the mechanical analysis as a predefined temperature field using the usual Abaqus commands directly in the input file or through the graphical interface.

During the mechanical analysis, the hygro-mechanical strain is calculated as a thermal strain by specifying the coefficient of hygroscopic swelling as the thermal expansion coefficient in the material properties, as it was done in this case. If one desires to conduct a coupled hygro-thermal mechanical analysis, that is also possible by importing the concentration values as a predefined field and using the user subroutine UEXPAN to define the coefficient of hygroscopic swelling and thermal expansion. An example of this approach is given in S. Yoon et. al.'s article [58].

4.3.2 Material Properties

In a finite element analysis is usual to take advantage of the symmetric properties, geometric and load-wise, to simplify the model and the computational effort. In this case, it was possible to only consider one fourth of the sample as shown on figure 4.1. The composites were also taken into account since the interaction between them and the adhesive was important for the mechanical analysis.

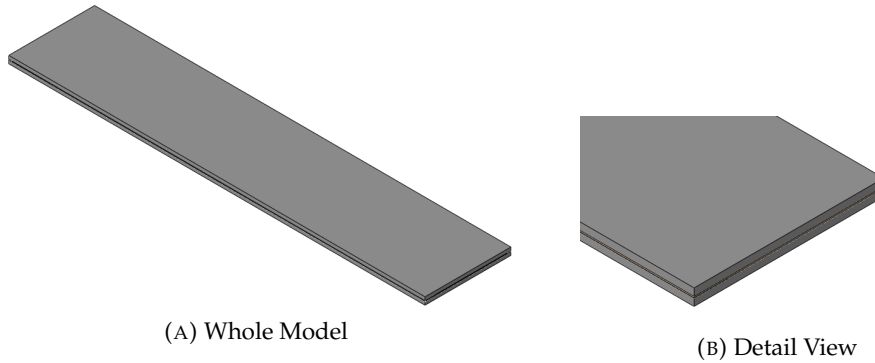


FIGURE 4.1: Model for Hygro-Mechanical Analysis

Table 4.1 lists the material properties for both the adhesive and the composites. The coefficient of hygroscopic swelling was determined by experimental data, since it is given by the slope when plotting strains values against concentration, as given by equation 4.1 and shown on figure 1.7.

The coefficient of hygroscopic swelling (CHS) is a material property, and as such, doesn't depend on the geometry. The experimental data shows, however, very different CHS values for Sample A and Sample B. It is still unclear why this is the case. For the analysis, in order to compare computed strains with experimental results, it was decided to use the corresponding theoretical CHS values for each sample as well.

Viscoelastic properties of the adhesive were not contemplated in the analysis. Expected tensile strain values are small enough that the material is kept in the elastic range, as shown by the stress-strain curve for Hysol EA-9394 adhesive [63].

TABLE 4.1: Material Properties - Hygro-Mechanical

Material	Parameter	Value	Units
Adhesive	Density	0.00136 [24]	g/mm^3
	Young's Modulus	$5.49 \text{ E}+16$ [24]	$(\text{g} \cdot \text{mm}/\text{s}^2)/\text{mm}^2$
	Poisson's Ratio	0.4 [63]	
	Coeff. Hygroscopic Swelling	0.004030 (A) 0.007685 (B)	
Composite	Density	0.00187 [30]	g/mm^3
	Young's Modulus	$4.17\text{E}+17$ [29]	$(\text{g} \cdot \text{mm}/\text{s}^2)/\text{mm}^2$
	Poisson's Ratio	0.3 [29]	

4.3.3 Boundary Conditions and Loads

Since only one fourth of the sample was used, symmetric boundary conditions were applied on the corresponding faces. Also, a condition of zero displacement in the y-axis was applied to the bottom surface since it's simply supported by the tray. Figure 4.2 shows the model with the faces where the conditions were applied.

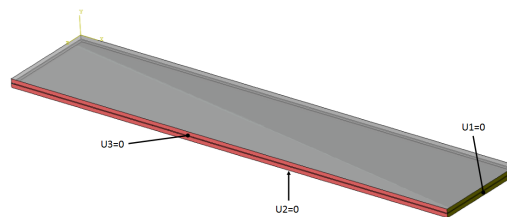


FIGURE 4.2: Boundary Conditions - Hygro-Mechanical

The weight of the composites on the adhesive was included in the analysis through the use of a gravity load. This is an in-built load in Abaqus. It is used to represent the gravitational acceleration. Abaqus applies the weight according to the geometry and density of the material. The inputs are the direction and the magnitude. In this case, since millimeters and hours were the units used, it has a value of $-1.27008\text{E}+11 \text{ mm/h}^2$ (9.81 m/s^2).

Another external force considered was the water pressure on top of the sample. As was explained on chapter 1 and 3, the samples were submerged in a tray with demineralised water. The column of water on top of the samples had a maximum height of 5 mm. Thus, the water pressure on top of the sample had a magnitude of $6.24\text{E}+08 \text{ g/mm h}^2$.

The moisture concentration distribution within the sample is the main driver for the deformation. This load was imported as a predefined field in the model. Concentration values are applied on each node according to the previously performed mass diffusion analysis. Two approaches were used for the concentration distribution: Time-Varying Boundary Conditions and the Dual-Stage model. Both results were used for the sequential mechanical analysis in separate simulations.

4.3.4 Interactions

The interaction between the composites and the adhesive was very important in the mechanical analysis. This interaction was defined as a contact interaction with tangential behaviour using a high frictional coefficient (0.9). The interaction was defined between the top surface of the bottom composite and the bottom surface of the adhesive; and between the bottom surface of the top composite and the top surface of the adhesive. This interaction was preferred over a tie constraint, since the latter would prove very restrictive. A frictional interaction was deemed more representative and since there's a chance of slippage between the surfaces, the composites were modelled as slightly larger than the adhesive.

4.3.5 Model Mesh

When a predefined field is imported, nodes in the mesh are assigned the respective values. To this end, it is advisable to keep the meshes between the analyses as similar as possible. If there's a mismatch between the meshes, the algorithm tries to interpolate values between nodes. Of course, this can introduce more variability in the study. For this analysis, it was preferred to keep identical meshes for the adhesive between analyses.

The mass diffusion analysis only considered the adhesive. In the hygro-mechanical analysis three part instances were considered: the adhesive, the top composite and the bottom composite. The use of more or less instances between analyses is not a problem when importing results for a predefined field. The program assigns the nodal values according to the name of the part. As long as each instance has the same name in both analysis, the use of other instances will not affect the results.

For the adhesive, two uniform meshes were used in the mass diffusion analysis, a coarse mesh of 1 mm elements and a finer mesh of 0.5 mm elements. During the mass diffusion analysis, the coarse mesh proved sufficient to obtain accurate results. In the case of the hygro-mechanical analysis, the finer 0.5 mesh provides a better element aspect ratio, 7.5 for Sample A and 3.5 for Sample B, which could lead to an improvement in results. Both meshes were used and results were compared.

Both meshes had a constraint of 3 elements for the thickness. This was done in order to have central elements where the FBG sensors were embedded in the samples. Element sets for both sensors were created in both samples to compare simulation results with experimental measurements. Figure 4.3 shows the location of the element sets defined on the 1 mm mesh.

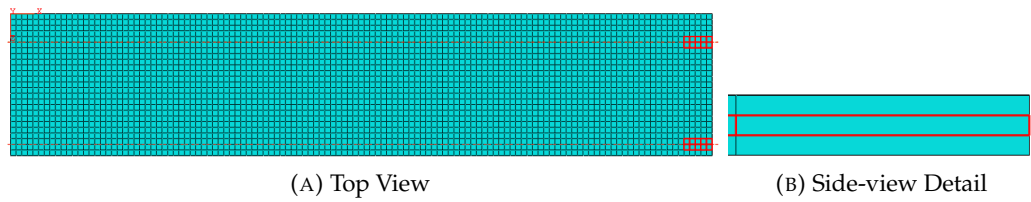


FIGURE 4.3: Sensor Element Sets - 1 mm Mesh

As for the composites, a coarse uniform mesh of 1 mm was imposed on both parts. The composites were not areas of interest in the analysis and a 1 mm mesh provides a good aspect ratio since both have a thickness of 1 mm.

All part instances were assigned 8-node linear brick elements with reduced integration (type C3D8R). Given the geometry of the sample, in which two dimensions are much larger than the third, the use of shell elements would have been, perhaps, more appropriate. However, the use of shell elements is not supported for a mass diffusion analysis, and so, it limited the use in the mechanical analysis since respective nodes were desired to be equal for the assigning of the predefined field. An alternative, would have been to use continuum shell elements, which take their thickness from the element nodal geometry, for the mechanical analysis only. Unfortunately, the constitutive relations for continuum shell elements in Abaqus are not equipped to handle temperature changes unless it is in a coupled thermal-displacement analysis [64].

4.4 Analysis Results

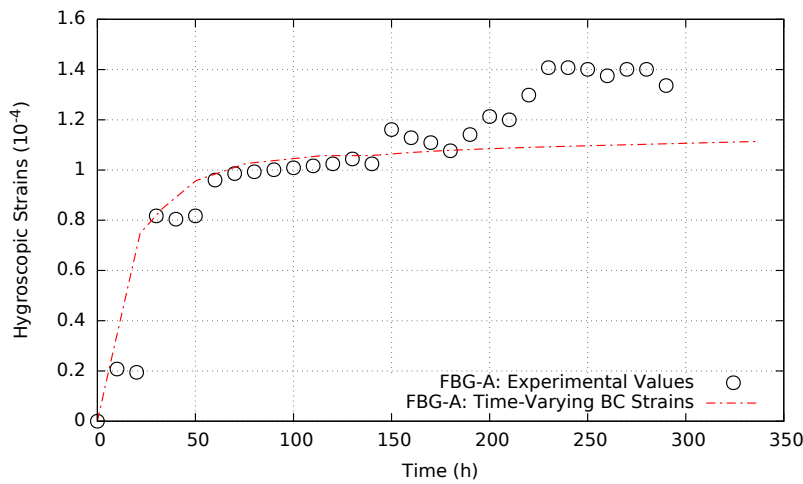
Fibre-Bragg Grating (FBG) sensors are sensitive to mechanical strains as well as to temperature changes. For this reason, their use has proliferated in structural health monitoring applications. In this experiment, FBG sensors were embedded in the adhesive layer of the sample and the wavelength measurements were used to calculate hygroscopic strains through equation 1.4. It's important to note that FBG sensors measure strains in the direction parallel to their axis.

A sequentially-coupled hygro-mechanical analysis was performed through the use of the finite element method. Two different approaches were used for the mass diffusion analysis: Time-Varying BC and Dual-Stage. Results from both mass diffusion approaches were implemented for the hygro-mechanical analysis. Strain profiles for each FBG sensor were compared to the experimental ones.

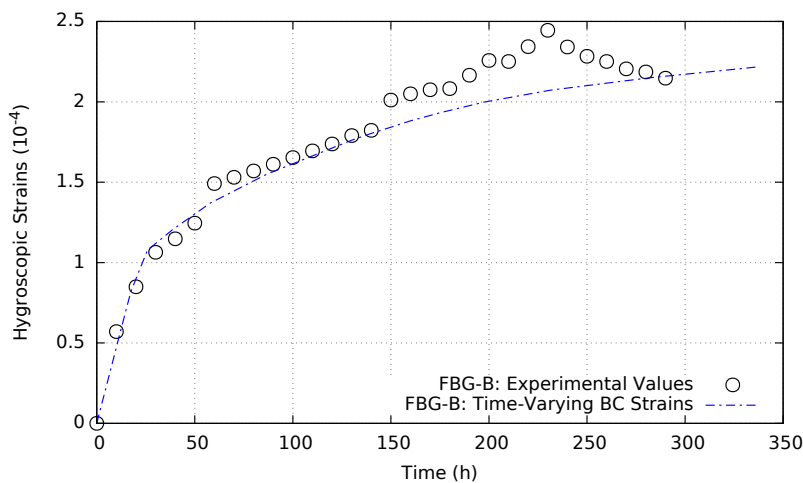
4.4.1 Time-Varying BC Strain Profiles

The Time-Varying Boundary Condition model takes into account the visco-elasticity effect on the diffusion mechanism through the use of time-dependent boundary condition based on a Prony series given on equation 3.7.

Two different samples were used for the experiment, Sample A and Sample B. Sample A has a thickness of 0.2 mm and a 10-mm FBG sensor placed near the center of the sample. Sample B has a thickness of 0.4 mm and a 10-mm FBG sensor closer to the edge of the sample. Strain profiles for the sensors corresponding to each sample are shown on figure 4.4.



(A) Sample A Sensor - Time-Varying BC

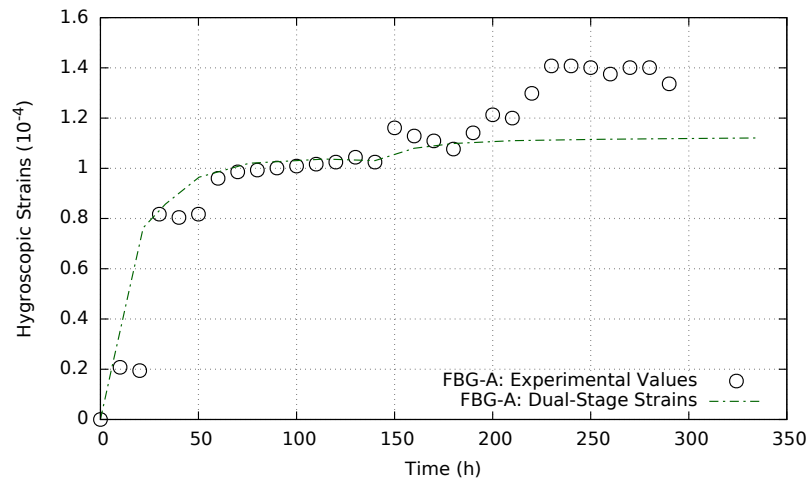


(B) Sample B Sensor - Time-Varying BC

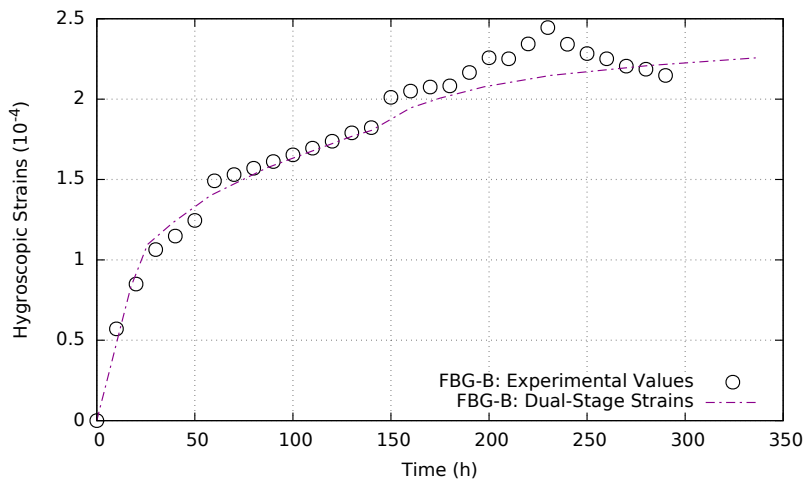
FIGURE 4.4: Time-Varying BC - Strain Profiles

4.4.2 Dual-Stage Strain Profiles

The Dual-Stage model proposes the analysis of the anomalous diffusion by characterizing it as the product of two sequential Fickian diffusion profiles with distinct saturation concentrations and diffusion coefficients. The strain profiles estimated for this approach and for each FBG sensor are displayed on figure 4.5. Figure 4.6 shows a comparison between the different approaches and different sensor areas.



(A) Sample A Sensor - Dual-Stage



(B) Sample B Sensor - Dual-Stage

FIGURE 4.5: Dual-Stage - Strain Profiles

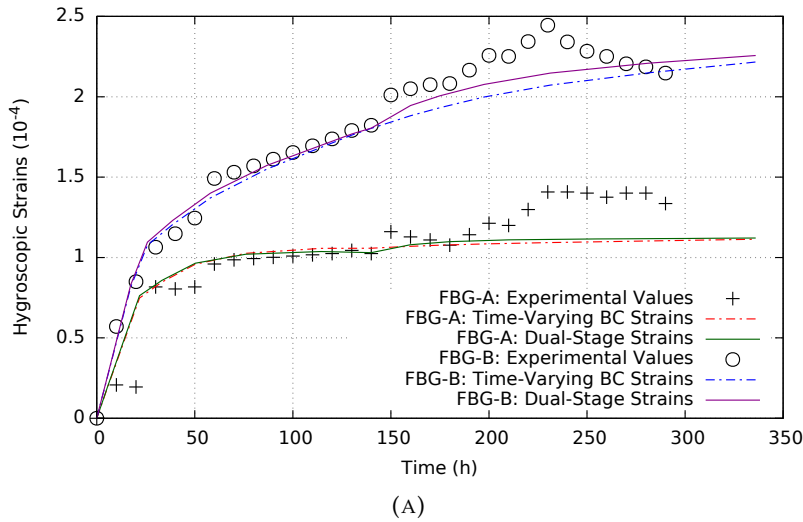
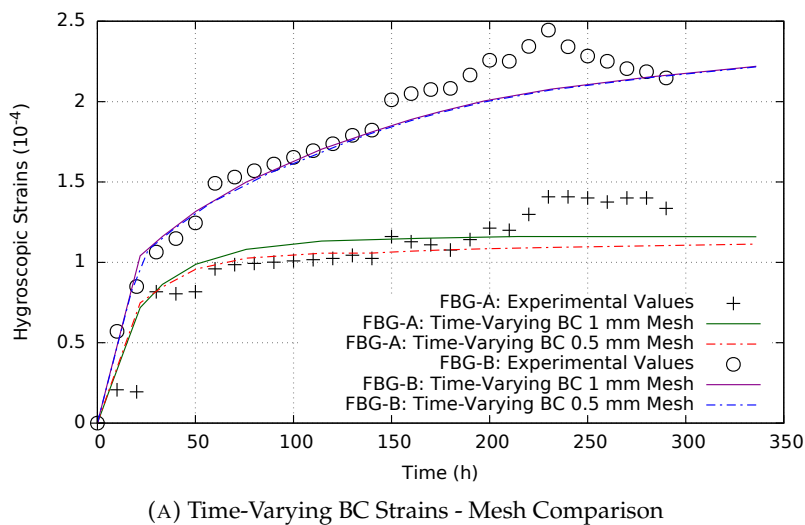
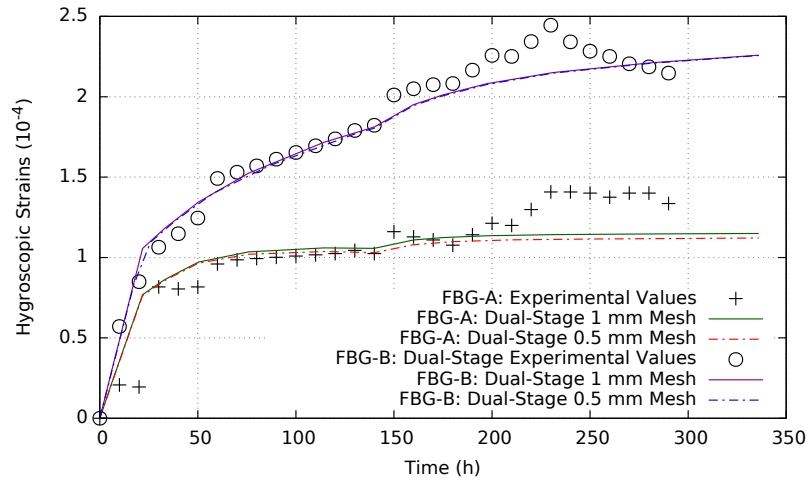


FIGURE 4.6: Strain Profile Comparison

4.4.3 1 mm vs 0.5 mm Mesh

The finite element method is a numerical method which tries to approximate the response of a continuum solid through the analysis of discrete sections of it. It is a numerical approximation, and as such, it is evident that the finer you discretize, the better the approximation. Of course, the use of more elements comes with an additional cost: computational time. In this case, two different meshes to partition the sample were used: 1 mm mesh and a 0.5 mm mesh. The results for the strain profiles for each different mesh per diffusion approach are shown on figure 4.6.





(B) Dual-Stage Strains - Mesh Comparison

FIGURE 4.6: Strain Profiles - Mesh Comparison

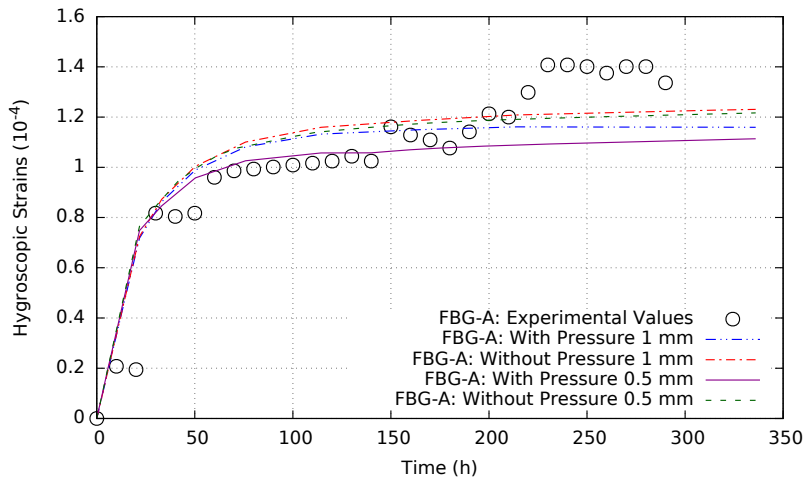
The computational time required by each analysis is detailed on table 4.2. Information is also given on the number of elements and nodes involved with each mesh size.

TABLE 4.2: Computational Times per Mesh Size

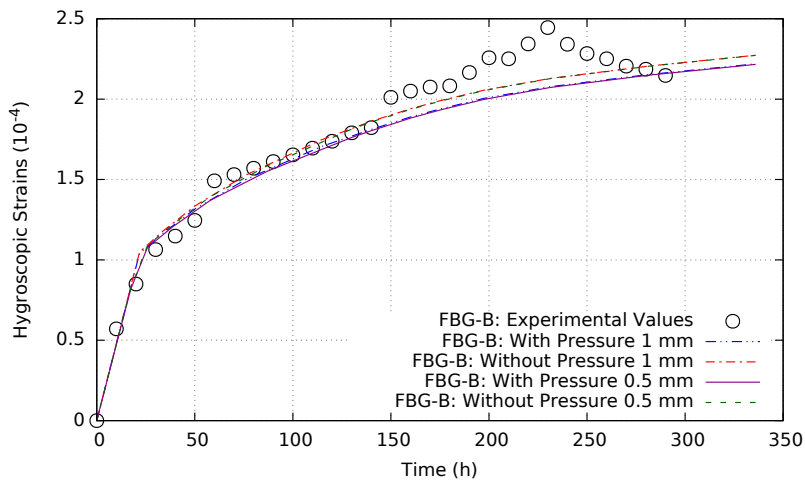
	Sample A		Sample B	
	1 mm	0.5 mm	1 mm	0.5 mm
Time-Varying	16 min	1 h 36 min	10 min	1 h 8 min
Dual-Stage	24 min	1 h 22 min	12 min	1 h
Problem Size	15 927 elem. (26 820 n.)	44 052 elem. (64 920 n.)	15 927 elem. (26 820 n.)	44 052 elem. (64 920 n.)

4.4.4 Water Pressure Effect

Both samples were placed inside a box and submerged in demineralise water. The column of water on top of both samples had a height of 5 mm. The pressure exerted by this column was considered as a load in the hygro-mechanical model. A separate set of simulations were ran without this pressure load to quantify the effect of the water pressure on the strain profiles. Results are shown on figures 4.7 and 4.8 .

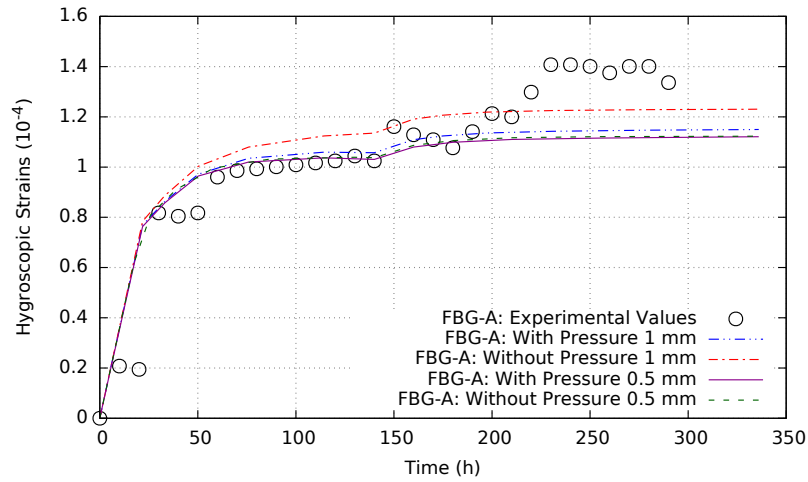


(A) Time-Varying BC Strains - Pressure Effect on A

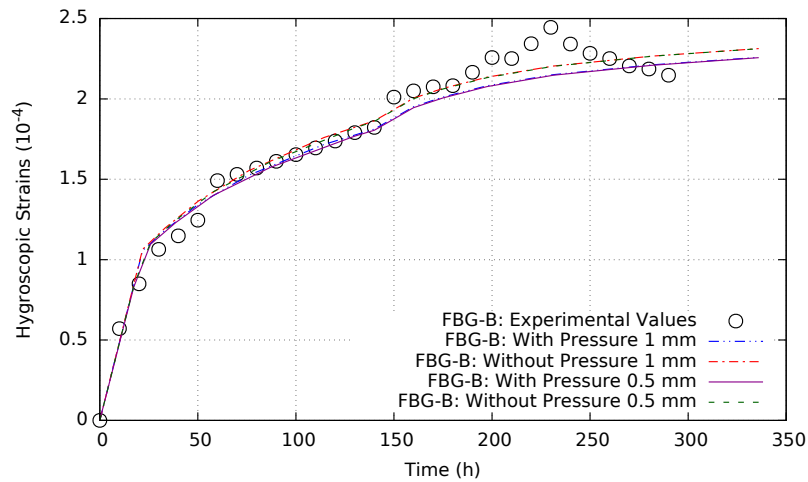


(B) Time-Varying BC Strains - Pressure Effect on B

FIGURE 4.7: Time-Varying BC - Pressure Effect



(A) Dual-Stage Strains - Pressure Effect on A



(B) Dual-Stage Strains - Pressure Effect on B

FIGURE 4.8: Dual-Stage Strains - Pressure Effect

4.5 Conclusions

The strains caused by moisture absorption in an adhesive joint between composites were determined by a sequentially-coupled hygro-mechanical analysis using a finite element model. The simulation results were compared to experimental values obtained through Fiber Bragg grating sensors embedded in adhesive layers with thicknesses of 0.2 and 0.4 mm.

The diffusion process through the polymeric material was modelled by two different approaches: the Time-Varying Boundary Condition and the Dual-Stage model. Figures 4.4 and 4.5 show the strains profiles from each approach, respectively; and figure 4.6 compares both approaches.

With the time-varying boundary condition approach, the mechanical strains show slightly higher values than the experimental results for the sensor in Sample A. The profile trend, nonetheless, does resemble the experimental strain profile during the first 150 hours. The difference could be attributed to the error involved in calculating the value for the coefficient of hygroscopic swelling (CHS), which was done by estimating the slope of the strain-concentration curve shown on figure 1.7. The strain profile for the sensor in Sample B with this approach, 4.4b, gives a better correlation with the experimental results.

In the case of the dual-stage model, strain profiles obtained for Samples A and B demonstrate a good correlation with the experimental results, during the first 200 hours. Both approaches used the same CHS values. The time between the stages in the dual-stage diffusion model, coincides with the increase of the experimental values. In this way, the dual-stage model is able to adapt better to the results than the time-varying boundary condition model.

Neither approach, however, follows the experimental profile trends on either one of the samples after the 200th hour of the simulation. In sample A, the experimental values show a steady increase from an approximate strain value of 0.00012 to 0.00014; with a slight decrease towards the end of the measurements. A much more quick increase is observed in Sample B, where the maximum strain value reached is 0.00024; followed immediately by a decrease.

During the experiment, all external conditions were kept constant. The only load varying with time was the amount of moisture entering the sample. The hygroscopic strains follow a linear relationship with the concentration difference, as stated in equation 4.1. A strain value of 0.00014 in sample A, would then imply a concentration of 3.47%, which is higher than the 3.126% measured from weight-gain absorption data (figure 3.5). The sudden increase and decrease shown by sample B, would imply a sudden higher diffusivity followed by a desorption process. Both samples were kept submerged for all measurements.

A change in temperature could affect the diffusivity coefficient in the samples and provoke thermal strains that weren't accounted for during the measurements with the dry sample (section 2.3.1). The samples were placed in a temperature chamber controlled and monitored at 60 ± 2 °C, throughout the experiment. Thermal strains can be calculated by equation 1.13. A 2°C increase in the temperature would account for an increase of only 0.0000183 in the strain value.

Experimental strain values were calculated by the changes in wavelength measured by the FBG sensors (equation 1.4). It is possible that during a wavelength measurement, the spectrum recorded by the FBG is not composed of only one clear peak but rather several peaks. The measurement equipment used,

takes the highest of the peaks and presents that as the measurement. This highest peak may not be representative of the sample. A comparison between spectra and wavelength could help determine if this is the case for the odd measurements presented in the strain profiles. Unfortunately, the measuring unit is able to record either wavelength or spectra only, not both simultaneously, so such a comparison was not available.

Simulations were performed using two different meshes for each sample: a 1 mm and a 0.5 mm mesh. The 0.5 mm mesh was thought to be better since it provided a better aspect ratio for the elements. However, as can be seen on figure 4.6, for the time-varying boundary condition simulations the obtained strain profiles from both meshes are basically identical. The same holds true for the strain profile for the sensor in sample B with the dual-stage approach. The only case where the use of a finer mesh is justified is with sample A with the dual stage approach. There's a noticeable difference between measurements. The finer mesh shows lower strain values that provide a better correlation with the experimental values during the first hours. Sample A with the dual-stage model could be more susceptible to a finer mesh than sample B because of its thinness. When compared to sample A with the time-varying boundary condition, the concentration profiles from both samples (figure 3.9) shows that the dual-stage model has more drastic changes in concentration that a finer mesh is able to adapt to better.

The use of a finer mesh always implies a higher computational time. Table 4.2 shows that the use of the 0.5 mm mesh increases the computational cost by an average factor of 5. This computational cost was only justified for one case, when the sample's focus area is closer to interaction zones and there's more variability in the loading conditions.

Lastly, the effects of the water column on the measurements were estimated by running simulations with and without considering it and then comparing the results. Results were obtained for different size meshes as well. When using the time-varying approach on sample A, figure 4.7a, the water column shows to have an effect with either size mesh, lowering the strain values. Differences between meshes are negligible if the water pressure is disregarded. If the water column is considered, the mesh size does play an important role showing higher strain values with a coarser mesh than with the finer mesh. Neglecting the water column effect with a 1 mm mesh shows a maximum difference of 0.000011691 (10.49 % increase).

For sample B, with the time-varying approach, mesh sizes don't create any differences as seen on figure 4.7b. The water pressure on the sample does lower the magnitude of the strain values from 0.000227176 to 0.000221605 (2.51 % decrease), most notably during the last hours of the simulation.

With the dual-stage approach, similar behaviours between same size samples are seen. When using the time-varying approach on sample A, figure 4.8a, the water column doesn't show any effect with a 0.5 mm mesh. On the other hand, with the 1 mm mesh, the effect is considerable. Disregarding the water pressure with a 1 mm mesh can lead to estimate strains 9.77% higher than in reality. Sample B remains unchanged with different meshes but is affected by the water column on top. Nonetheless, the water effect on sample B creates a small difference of 5.62E-06 (2.49 % decrease) between strain values.

Chapter 5

Summary

5.1 Introduction

This project was motivated by the experimental results obtained by a research team at the Institute of Fluid-Flow Machinery in Gdańsk, Poland. The experiment consisted of three samples of adhesive joints between composites that were submerged in water for a period of 336 hours. The goal of the research was to quantify the moisture-induced strains on the adhesive joint and prove the feasibility of using Fiber Bragg Grating (FBG) sensors for such a purpose.

Due to the polymeric nature of adhesives, moisture content in the surroundings of an adhesive joint can be absorbed and have a detrimental effect on the mechanical strength of the bond. Lack of a complete understanding of these dynamics, limits the use of adhesive joints in many applications where a faulty adhesion may pose a safety hazard.

FBG sensors embedded in adhesive joints could be used in structural health monitoring applications, as a way to profit from the versatility and many advantages of adhesives in a manner that won't risk public safety.

The goal of the present project was successfully reached by creating numerical models that could represent the thermal response, mass diffusion dynamics and moisture-induced strain propagation of the samples used. Three separate finite-element models were created: a transient thermal analysis, a transient mass diffusion analysis and a hygro-mechanical analysis.

5.1.1 Thermal Analysis

FBG sensors are both sensitive to mechanical strains as well as temperature changes. Since the moisture-induced strains, also referred to as hygroscopic strains, were the focus of the experiment, temperature's effect on the measurements had to be quantified and considered.

One sample, labelled as sample A, was placed in a temperature chamber at 60°C in dry conditions, to quantify the strains produced by the temperature

change and assess the time it took the sample to reach thermal equilibrium. Afterwards, samples A and B were placed in the same temperature chamber completely immersed in water. Temperature was kept constant so that all following measurements could be associated directly to hygroscopic strains.

The thermal model was constructed to simulate the temperature distribution of Sample A when inside the chamber in dry conditions and also when samples A and B were inside the chamber in wet conditions.

When in dry conditions, the thermal model was able to accurately simulate the temperature profile obtained by the FBG sensor embedded in the sample. Experimental values were not collected for the temperature profiles for when the samples A and B were submerged.

During the experiment, the samples had to be taken out of the water and be weighed outside of the temperature chamber. Mathematical models for this situation were created in order to verify the assumption that all strain measurements were done under an isothermal state. Simulations results show that both samples, in spite of the difference in thickness, are able to reach thermal equilibrium within the first 5 minutes. There were hours of difference between the weight measurements and the strain readings. Thus, one can conclude that, even when considering the error involved in the calculation of the convection coefficient, both samples were in an isothermal state when the strain measurements were recorded.

5.1.2 Mass Diffusion Analysis

At the moment the samples are submerged, a diffusion process is started in which water penetrates inside the sample until it reaches a saturation point. The concentration distribution of moisture inside the adhesive of both samples was essential to properly simulate the hygroscopic strains.

During the experiment, sample A was periodically weighed to determine the overall level of moisture concentration and determine the saturation point.

Mass diffusion processes, in many materials, can be mathematically analysed through Fick's equations of diffusion, which hold a strong analogy to heat transfer equations. Polymeric materials, however, have shown not to follow the diffusion profiles predicted by Fickian equations.

Different mathematical models have been created to better understand the diffusion dynamics in polymers such as adhesives. In the present project, two different approaches were implemented: time-varying boundary conditions and the dual stage model. Results from both approaches used in samples A and B, were produced and compared.

The main drawback from either one of these approaches, and also from Fickian equations, is that they all use variables obtained from experimental values. When comparing the overall concentration of sample A from both approaches with experimental data, the time-varying boundary condition shows a better correlation than the dual-stage model. However, the time-varying boundary condition model requires the adjustment of variables to provide the best fit. The dual-stage model requires less information from experimental results. Nonetheless, the dual-stage model also presents a good correlation with results.

5.2 Hygro-mechanical Analysis

The main focus of the project was to predict the hygroscopic strains inside the adhesive layers in samples A and B. To this effect, a sequentially coupled hygro-mechanical analysis was conducted.

With the mass diffusion analysis, average concentration of the whole sample was calculated to compare with experimental results. Yet, the most important result was the concentration distribution within the sample and its progression with time. These spatial-concentration results were imported into a mechanical analysis to simulate the swelling effect of moisture absorption. Results from both mass diffusion approaches were used.

Strain measurements taken by the FBG sensors correspond to very localised areas inside the adhesive. Sets of elements from the FE model were taken from these areas in the samples and results were compared to experimental values.

Both approaches are able to follow the strain profile up to the 200th hour. The dual-stage model shows better correlation with results in general, especially for the strain increase in sample B around the 150th hour of simulation.

Unfortunately, after the 200th hours, experimental values show a profile that neither model can simulate. Experimental strain values show an unlikely increase. Considering the linear relationship between hygroscopic strains and moisture, experimental strain results on sample A seem to indicate a concentration value of 3.47%, much higher than the saturation point of 3.126 %.

All loading conditions were kept constant throughout the experiment. Temperature was controlled by the temperature chamber and kept at $60 \pm 2^\circ\text{C}$. A temperature variation could affect diffusivity and create thermal strains. However, a 2°C variation would only account for an increase of 0.0000183 in the strain values which is not enough for the results obtained.

Experimental strain values were calculated by the changes in wavelength measured by the FBG sensors. It's a possibility that during a wavelength measurement, the spectrum recorded by the FBG was not composed of only one

clear peak but rather several peaks. The measurement equipment used, takes the highest of the peaks and presents that as the measurement. This highest peak may not be representative of the sample. A comparison between spectra and wavelength could help determine if this is the case for the odd measurements presented in the strain profiles. Unfortunately, the measuring unit is able to record either wavelength or spectra only, not both simultaneously, so such a comparison is not available.

The FE models created for the hygro-mechanical show a good correlation with experimental results for 60% of the simulation time. The reasons for the incongruences towards the end of the simulation remain unknown. It may be that the mathematical models used for moisture diffusion in the sample are not able to completely represent the diffusion process, yet, good correlation with sample concentration was obtained with both approaches. Unaccounted loading conditions during experimental measurements could have also affected the strain profiles, or perhaps variabilities within the measuring equipment. Nonetheless, in both those cases, there's lack of information to corroborate.

5.3 Future Works

All the analyses conducted to study the thermal, mass diffusion and hygro-mechanical responses of the samples are explained thoroughly in the present project so the methodology followed can be implement in further experiments.

Given the fact that the simulation results weren't able to explain the experimental strain profiles for the last hours of the experiment; new experimental data is needed to verify if the erratic behaviour is due to the model or to unaccounted factors during the measurement of this particular set of values.

Within the context of the research efforts at the Institute of Fluid-Flow Machinery, the 3D finite element models created give an approximation to the diffusion and swelling effects that are taking place along the whole sample as opposed to only focalized areas where experimental values can be obtained. The representation of the concentration distribution provides good guidance as to where would be best to place sensors for future experiments. Also, the finite elements models, will serve as a basis for furthering the research into the special dynamics taking place between the adhesive and composite layers and the degradation of the joint in these areas.

Appendix A

User Subroutine - UFIELD

```
          SUBROUTINE UFIELD(FIELD,KFIELD,NSECPT,KSTEP,KINC,  
1          TIME,NODE,COORDS,TEMP,DTEMP,NFIELD)  
C  
          INCLUDE 'ABA_PARAM.INC'  
C  
          DIMENSION FIELD(NSECPT,NFIELD),COORDS(3),  
1          TIME(2),TEMP(NSECPT), DTEMP(NSECPT)  
C  
          FIELD(1,1)=TIME(2)  
C  
          RETURN  
          END
```


Appendix B

Average Concentration - Python Script

Python scripts can be run within the Abaqus environment for post-processing purposes. The following is a python code developed to calculate the average concentration of the whole model according to equation 3.24.

More information on the functions and variables used in this code is available in Abaqus documentation: Abaqus Scripting User's Guide and Abaqus Scripting Reference Guide [65, 66].

```
# Average Concentration with time
from odbAccess import *
from abaqusConstants import *

odb = openOdb(path='505a.odb')
endSet = odb.rootAssembly.instances['ADHESIVE3D-1']

myFile = open('AveConc-505a.txt', 'w+')
myFile.write("# Time Vol Sum ISOL Sum Ave Conc \ n")

for step in odb.steps.values():
    numFrame = len(step.frames)
    for fr in range(0, numFrame):
        frame = step.frames[fr]

        Vfield = frame.fieldOutputs['IVOL']
        VsubField = Vfield.getSubset(region=endSet)

        Sfield = frame.fieldOutputs['ISOL']
        SsubField = Sfield.getSubset(region=endSet)
        Ssum = 0
```

```
Vsum = 0

for num in range(len(VsubField.values)):
    Vval = VsubField.values[num].data
    Vsum = Vsum + Vval
    Sval = SsubField.values[num].data
    Ssum = Ssum + Sval

ave = Ssum / Vsum
frametotalTime = step.totalTime + frame.frameValue

myFile.write(str(frametotalTime))
myFile.write(" ")
myFile.write(str(Vsum))
myFile.write(" ")
myFile.write(str(Ssum))
myFile.write(" ")
myFile.write(str(ave))
myFile.write("text\ n")

myFile.close()
```


Appendix C

Record Key Change Code

The following code was taken from the article by S. Yoon, C. Jang and B. Han entitled "Nonlinear stress modeling scheme to analyze semiconductor packages subjected to combined thermal and hygroscopic loading" [58].

```
SUBROUTINE ABQMAIN

INCLUDE 'aba_param.inc'
DIMENSION ARRAY(513), JRRAY(NPRECD,513)
EQUIVALENCE (ARRAY(1),JRRAY(1,1))

PARAMETER (MXUNIT = 21)
INTEGER LRUNIT(2,MXUNIT),LUNIT(10)
CHARACTER FNAME*80
DATA LUNIT/1,5,6,7,9,11,12,13,20,28/

NRU=1
LOUTF=2
LRUNIT(1,1)=8
LRUNIT(2,1)=2

WRITE(6,60)
60 FORMAT(1X,'Enter the name of the input file(s) (w/o extension):')
READ(5, '(A)') FNAME
CALL INITPF(FNAME, NRU, LRUNIT, LOUTF)
JUNIT = 8
KEYPRV = 0

DO 110 INRU = 1, NRU
  JUNIT = LRUNIT(1,INRU)
```

```

CALL DBRNU (JUNIT)
I2001 = 0
DO 100 IXX2 = 1, 100
  DO 80 IXX = 1, 99999
    CALL DBFILE(0,ARRAY,JRCD)
C  WRITE(6,*)'KEY/RECORD LENGTH=', JRRAY(1,2), JRRAY(1,1)
    IF (JRCD .NE. 0 .AND. KEYPRV .EQ. 2001) THEN
      WRITE(6,*) 'END OF FILE # ', INRU
      CLOSE (JUNIT)
      GOTO 110
    ELSE IF (JRCD .NE. 0) THEN
      WRITE(6,*) 'ERROR READING FILE # ', INRU
      CLOSE(JUNIT)
      GOTO 110
    ENDIF

LWRITE = 1

IF (INRU.GE.1) THEN
  IF (JRRAY(1,2).GE.1900 .AND. JRRAY(1,2).LE.1909) LWRITE=0
  IF (JRRAY(1,2).GE.1912 .AND. JRRAY(1,2).LE.1922) LWRITE=0
  IF (JRRAY(1,2).EQ.2001 .AND. I2001.EQ.0) THEN
    I2001= 1
    LWRITE=0
  ENDIF
ENDIF

IF(INRU .EQ. 1 .OR. LWRITE .EQ. 1) THEN
  KEY = JRRAY(1,2)

  IF ((KEY.EQ.1900) .OR. (KEY.EQ.1901) .OR. (KEY.EQ.1902) .OR.
1  (KEY.EQ.1910) .OR. (KEY.EQ.1911) .OR. (KEY.EQ.1921) .OR.
2  (KEY.EQ.1922) .OR. (KEY.EQ.1980) .OR. (KEY.EQ.2000) .OR.
3  (KEY.EQ.2001) .OR. (KEY.EQ.1)) THEN
    CALL DBFILW (1, ARRAY,JRCD)
    IF (JRCD .NE. 0) THEN
      WRITE (6,*) 'ERROR WRITING FILE'
      CLOSE (JUNIT)
      GOTO 110
    
```

```
ENDIF
C
C If a current RECORD KEY is 221, the key is changed
C into 201 and the associated dataC are written to an output file.
C
ELSE IF ( (KEY.EQ.221 ) ) THEN
  JRRAY (1,2 ) =201
  CALL DBFILW (1, ARRAY, JRCD )
  IF (JRCD .NE. 0) THEN
    WRITE (6,*) 'ERROR WRITING FILE'
    CLOSE (JUNIT )
    GOTO 110
  ENDIF
ENDIF
ENDIF
ENDIF
KEYPRV = JRRAY(1,2)
80  CONTINUE
100 CONTINUE
110 CONTINUE
CLOSE(9)
C
RETURN
END
```


Bibliography

- [1] Mar-Bal Incorporated. *History of Composites*. 2016. URL: <http://www.mar-bal.com/language/en/applications/history-of-composites/> (visited on 07/07/2016).
- [2] C. Mitchell, L. Dangora, and J. Sherwood. "Investigation into a robust finite element model for composite materials". In: *Finite Elements in Analysis and Design* 115 (2016), pp. 1–8.
- [3] S. Eslami, A. Honarbakhsh-Raouf, and S. Eslami. "Effects of moisture absorption on degradation of E-glass fiber reinforced Vinyl Ester composite pipes and modelling of transient moisture diffusion using finite element analysis". In: *Corrosion Science* 90 (2015), pp. 168–175.
- [4] P.D. Mangalgi. "Composite materials for aerospace applications". In: *Bulletin of Materials Science* 22.3 (1999), pp. 657–664.
- [5] M. Scholz et al. "The use of composite materials in modern orthopaedic medicine and prosthetic devices: a review". In: *Composites Science and Technology* 71.16 (2011), pp. 1791–1803.
- [6] W.C. De Goeij, M.J.L. Van Tooren, and A. Beukers. "Composite adhesive joints under cyclic loading". In: *Materials & design* 20.5 (1999), pp. 213–221.
- [7] J.K. Kim, H.S. Kim, and D. Lee. "Investigation of optimal surface treatments for carbon/epoxy composite adhesive joints". In: *Journal of adhesion science and technology* 17.3 (2003), pp. 329–352.
- [8] L. da Silva, A. Öchsner, and R. Adams. *Handbook of adhesion technology*. Springer Science & Business Media, 2011.
- [9] X.J. Fan, S.W.R. Lee, and Q. Han. "Experimental investigations and model study of moisture behaviors in polymeric materials". In: *Microelectronics Reliability* 49.8 (2009), pp. 861–871.
- [10] C.E. Browning, G.E. Husman, and J.M. Whitney. "Moisture effects in epoxy matrix composites". In: *Composite Materials: Testing and Design (Fourth Conference)*. ASTM International. 1977.
- [11] R.J. Morgan, J.E. O'neal, and D.L. Fanter. "The effect of moisture on the physical and mechanical integrity of epoxies". In: *Journal of Materials Science* 15.3 (1980), pp. 751–764.
- [12] M. Mieloszyk and W. Ostachowicz. "Moisture contamination detection in adhesive bond using embedded FBG sensors". In: *Mechanical Systems and Signal Processing* (2016).
- [13] A. Othonos and K. Kalli. *Fiber Bragg gratings: fundamentals and applications in telecommunications and sensing*. Artech House, 1999.

- [14] A. Othonos. "Fiber bragg gratings". In: *Review of scientific instruments* 68.12 (1997), pp. 4309–4341.
- [15] L. da Silva, P. Moreira, and A. Loureiro. "Determination of the strain distribution in adhesive joints using fiber Bragg grating (FBG)". In: *Journal of Adhesion Science and Technology* 28.14-15 (2014), pp. 1480–1499.
- [16] K. Hill and G. Meltz. "Fiber Bragg grating technology fundamentals and overview". In: *Journal of lightwave technology* 15.8 (1997), pp. 1263–1276.
- [17] J.A. Guemes and J.M. Menendez. "Response of Bragg grating fiber-optic sensors when embedded in composite laminates". In: *Composites science and technology* 62.7 (2002), pp. 959–966.
- [18] G Luyckx et al. "Strain measurements of composite laminates with embedded fibre Bragg gratings: Criticism and opportunities for research". In: *Sensors* 11.1 (2010), pp. 384–408.
- [19] G.B. Hocker. "Fiber-optic sensing of pressure and temperature". In: *Applied optics* 18.9 (1979), pp. 1445–1448.
- [20] F. Bosia et al. "Characterization of the response of fibre Bragg grating sensors subjected to a two-dimensional strain field". In: *Smart materials and Structures* 12.6 (2003), p. 925.
- [21] Y-J Rao. "Fiber Bragg grating sensors: principles and applications". In: *Optical fiber sensor technology*. Springer, 1998, pp. 355–379.
- [22] K. Sugden et al. "Fabrication and characterization of bandpass filters based on concatenated chirped fiber gratings". In: *Journal of Lightwave Technology* 15.8 (1997), pp. 1424–1432.
- [23] Institute of Fluid-Flow Machinery. *Centre of Mechanics of Machines*. 2016. URL: <http://www.imp.gda.pl/en/o4/> (visited on 07/07/2016).
- [24] Henkel Corporation. *LOCTITE EA 9394 AERO*. 2013. URL: <http://na.henkel-adhesives.com/product-search-1554.htm?nodeid=8797801054209> (visited on 03/26/2016).
- [25] P. Nithiarasu, R. Lewis, and K. Seetharamu. *Fundamentals of the finite element method for heat and mass transfer*. John Wiley & Sons, 2016.
- [26] A.E. Green and P.M. Naghdi. "A general theory of an elastic-plastic continuum". In: *Archive for rational mechanics and analysis* 18.4 (1965), pp. 251–281.
- [27] Dassault Systèmes Simulia Corp. "2.11 Heat Transfer". In: *Abaqus Theory Guide* ().
- [28] M. Lai et al. "An experimental–numerical study of moisture absorption in an epoxy". In: *Composites Part A: Applied Science and Manufacturing* 43.7 (2012), pp. 1053–1060.
- [29] T. Keller, C. Tracy, and A. Zhou. "Structural response of liquid-cooled GFRP slabs subjected to fire–Part I: Material and post-fire modeling". In: *Composites Part A: Applied Science and Manufacturing* 37.9 (2006), pp. 1286–1295.

- [30] Y. Bai, T. Vallée, and T. Keller. "Modeling of thermal responses for FRP composites under elevated and high temperatures". In: *Composites Science and Technology* 68.1 (2008), pp. 47–56.
- [31] R. Simons. "Simplified formula for estimating natural convection heat transfer coefficient on a flat plate". In: *Electronics Cooling Magazine* 8.1 (2002).
- [32] L. Jiji. *Heat convection*. Springer, 2006.
- [33] The Engineering Toolbox. *Water - Thermal properties*. 2016. URL: http://www.engineeringtoolbox.com/water-thermal-properties-d_162.html (visited on 07/26/2016).
- [34] The Engineering Toolbox. *Air Properties*. 2016. URL: http://www.engineeringtoolbox.com/air-properties-d_156.html (visited on 07/26/2016).
- [35] A. Jaffer. *Convection from a rectangular plate*. 2016. URL: <http://people.csail.mit.edu/jaffer/SimRoof/Convection/> (visited on 07/26/2016).
- [36] Y. Weitsman. *Fluid effects in polymers and polymeric composites*. Springer Science & Business Media, 2011.
- [37] E. Stellrecht, B. Han, and M. Pecht. "Characterization of hygroscopic swelling behavior of mold compounds and plastic packages". In: *IEEE Transactions on components and Packaging Technologies* 27.3 (2004), pp. 499–506.
- [38] L. Canal and V. Michaud. "Micro-scale modeling of water diffusion in adhesive composite joints". In: *Composite Structures* 111 (2014), pp. 340–348.
- [39] J. Crank. *The mathematics of diffusion*. Oxford university press, 1979.
- [40] S. Yoon, B. Han, and Z. Wang. "On moisture diffusion modeling using thermal-moisture analogy". In: *Journal of Electronic Packaging* 129.4 (2007), pp. 421–426.
- [41] F. Ellyin and R. Maser. "Environmental effects on the mechanical properties of glass-fiber epoxy composite tubular specimens". In: *Composites Science and Technology* 64.12 (2004), pp. 1863–1874.
- [42] F. Müller-Plathe, S. Rogers, and W.F. van Gunsteren. "Computational evidence for anomalous diffusion of small molecules in amorphous polymers". In: *Chemical physics letters* 199.3-4 (1992), pp. 237–243.
- [43] A. Mubashar et al. "Modelling cyclic moisture uptake in an epoxy adhesive". In: *The Journal of Adhesion* 85.10 (2009), pp. 711–735.
- [44] G. LaPlante, A. Ouriadov, and B.J. Lee-Sullivan P. Balcom. "Anomalous moisture diffusion in an epoxy adhesive detected by magnetic resonance imaging". In: *Journal of applied polymer science* 109.2 (2008), pp. 1350–1359.
- [45] H. Carter and K. Kibler. "Langmuir-type model for anomalous moisture diffusion in composite resins". In: *Journal of Composite Materials* 12.2 (1978), pp. 118–131.

- [46] L-W Cai and Y. Weitsman. "Non-Fickian moisture diffusion in polymeric composites". In: *Journal of composite materials* 28.2 (1994), pp. 130–154.
- [47] H Shirangi et al. "Characterization of dual-stage moisture diffusion, residual moisture content and hygroscopic swelling of epoxy molding compounds". In: *Thermal, Mechanical and Multi-Physics Simulation and Experiments in Microelectronics and Micro-Systems, 2008. EuroSimE 2008. International Conference on*. IEEE. 2008, pp. 1–8.
- [48] MH Shirangi and B Michel. "Mechanism of moisture diffusion, hygroscopic swelling, and adhesion degradation in epoxy molding compounds". In: *Moisture Sensitivity of Plastic Packages of IC Devices*. Springer, 2010, pp. 29–69.
- [49] Dassault Systèmes Simulia Corp. "6.9.1 Mass Diffusion Analysis". In: *Abaqus Analysis User's Guide* (2016).
- [50] Dassault Systèmes Simulia Corp. "2.13 Mass Diffusion". In: *Abaqus Theory Guide* (2016).
- [51] D. Karalekas, J. Cugnoni, and J. Botsis. "Monitoring of hygrothermal ageing effects in an epoxy resin using FBG sensor: A methodological study". In: *Composites science and technology* 69.3 (2009), pp. 507–514.
- [52] J. Zhou. "Sequentially-coupled finite element transient analysis with hygroscopic swelling". In: *EuroSime 2006-7th International Conference on Thermal, Mechanical and Multiphysics Simulation and Experiments in Micro-Electronics and Micro-Systems*. IEEE. 2006, pp. 1–6.
- [53] D.L. Vanderhart, M.A. Schen, and G.T. Davis. "Partitioning of water between voids and the polymer matrix in a polymer compound by proton NMR: the role of larger voids in the phenomena of popcorning and delamination". In: *Int. J. Microcircuits Electron. Packag* 22.4 (1999), pp. 423–441.
- [54] C. Toprak, J.N. Agar, and M. Falk. "State of water in cellulose acetate membranes". In: *Journal of the Chemical Society, Faraday Transactions 1: Physical Chemistry in Condensed Phases* 75 (1979), pp. 803–815.
- [55] L. El-Sa'ad, M.I. Darby, and B. Yates. "Moisture absorption by epoxy resins: the reverse thermal effect". In: *Journal of Materials Science* 25.8 (1990), pp. 3577–3582.
- [56] M.J. Adamson. "Thermal expansion and swelling of cured epoxy resin used in graphite/epoxy composite materials". In: *Journal of Materials Science* 15.7 (1980), pp. 1736–1745.
- [57] H. Ardebili, E.H. Wong, and M. Pecht. "Hygroscopic swelling and sorption characteristics of epoxy molding compounds used in electronic packaging". In: *IEEE Transactions on Components and Packaging Technologies* 26.1 (2003), pp. 206–214.
- [58] S. Yoon, C. Jang, and B. Han. "Nonlinear stress modeling scheme to analyze semiconductor packages subjected to combined thermal and hygroscopic loading". In: *Journal of Electronic Packaging* 130.2 (2008), p. 024502.

- [59] M.Y. Tsai et al. "An approach to determining residual strains and moisture diffusion coefficients of cured adhesives in electronic packaging". In: *ASME 2007 InterPACK Conference collocated with the ASME/JSME 2007 Thermal Engineering Heat Transfer Summer Conference*. American Society of Mechanical Engineers. 2007, pp. 711–717.
- [60] A. Lucantonio, P. Nardinocchi, and L. Teresi. "Transient analysis of swelling-induced large deformations in polymer gels". In: *Journal of the Mechanics and Physics of Solids* 61.1 (2013), pp. 205–218.
- [61] J-B Pyo et al. "Prediction of time-dependent swelling of flexible polymer substrates using hygro-mechanical finite element simulations". In: *Soft matter* 12.18 (2016), pp. 4135–4141.
- [62] S. Yoon et al. "Experimental verification of non-linear finite element analysis for combined hygroscopic and thermo-mechanical stresses". In: *Proceedings of 2005 SEM Annual Conference*. 2005.
- [63] TR Guess, ED Reedy, and ME Stavig. "Mechanical properties of hysol EA-9394 structural adhesive". In: *SAND95-0229, Sandia National Laboratories, Albuquerque, New Mexico* (1995).
- [64] Dassault Systèmes Simulia Corp. "29.6 Shell Elements". In: *Abaqus Analysis User's Guide* (2016).
- [65] Dassault Systèmes Simulia Corp. *Abaqus Scripting Reference Guide*. 2016. URL: <http://50.16.225.63/v2016/books/ker/default.htm>.
- [66] Dassault Systèmes Simulia Corp. *Abaqus Scripting User's Guide*. 2016. URL: <http://50.16.225.63/v2016/books/cmd/default.htm>.

List of Figures

1.1	Fiber Bragg Grating Sensor Diagram [18]	3
1.2	Sample Dimensions [12]	5
1.3	FBG sensor placement [12]	5
1.4	Moisture Weight Gain (%)	6
1.5	FBG sensors temperature measurements [12]	7
1.6	Moisture-induced strains on A and B Samples [12]	8
1.7	Moisture-induced strains vs water concentration [12]	9
2.1	Section of Sample Considered	13
2.2	Refined mesh on model	15
2.3	Sample A - Dry Conditions	16
2.4	Temperature Profiles	17
2.5	Sample A and B - Wet Conditions	18
2.6	Sample A and B Temperature Comparison	19
3.1	Schematic curves non-Fickian diffusion in polymers [36]	23
3.2	Dual-Stage on Experimental Data	28
3.3	Diffusion Analysis - Only External Faces	31
3.4	Sample mesh	31
3.5	Average Concentration - Experimental results	32
3.6	Average Concentration - Whole Sample	33
3.7	Comparison Fickian Profile	33
3.8	Mesh Comparison	34
3.9	Average Concentration - Sample Comparison	35
3.10	Sensor Area Comparison	36
3.11	Concentration Distribution at 336 h	36
3.12	Concentration Distribution Progression	39
4.1	Model for Hygro-Mechanical Analysis	44
4.2	Boundary Conditions - Hygro-Mechanical	45
4.3	Sensor Element Sets - 1 mm Mesh	47
4.4	Time-Varying BC - Strain Profiles	48
4.5	Dual-Stage - Strain Profiles	49
4.6	Strain Profile Comparison	50
4.6	Strain Profiles - Mesh Comparison	51
4.7	Time-Varying BC - Pressure Effect	52
4.8	Dual-Stage Strains - Pressure Effect	53

List of Tables

1.1	Adhesive Properties	6
2.1	Material Properties - Thermal Analysis	14
2.2	Parameters for Equation 2.9	15
3.1	Material Properties - Time-Varying BC	28
3.2	Material Properties - Dual Stage	29
3.3	Boundary Condition Parameters	30
3.4	Computational Times per Mesh Size	34
4.1	Material Properties - Hygro-Mechanical	44
4.2	Computational Times per Mesh Size	51